JOURNAL OF PETROLOGY

Journal of Petrology, 2015, Vol. 56, No. 5, 869–892
doi: 10.1093/petrology/egv020
Advance Access Publication Date: 25 May 2015
Original Article

OXFORD

A Simple Thermodynamic Model for Melting of Peridotite in the System NCFMASOCr

Eleanor S. Jennings* and Tim J. B. Holland

Department of Earth Sciences, University of Cambridge, Cambridge CB2 3EQ, UK

*Corresponding author: Telephone: +44 (0)1223 333424. E-mail: esj26@cam.ac.uk

Received August 21, 2014; Accepted April 3, 2015

ABSTRACT

A new thermodynamic model is presented for calculating phase relations in peridotite, from 0·001 to 60 kbar and from 800°C to liquidus temperatures, in the system NCFMASOCr. This model system is large enough to simulate phase relations and melting of natural peridotite and basaltic liquids. Calculations in the program THERMOCALC illustrate mantle phase relationships and melting conditions, specifically for the peridotite composition KLB-1. The garnet–spinel transition zone intersects the solidus at 21·4–21·7 kbar, where both Fe^{3+} and Cr increase spinel stability, expanding the width of the transition. Orthopyroxene is lost at the solidus at 42 kbar in KLB-1, although this pressure is very sensitive to bulk composition. Calculated oxidation states are in excellent agreement with measured log fO_2 for xenolith suites with mantle Fe_2O_3 contents in the range 0·1–0·3 wt %. It appears that mantle oxidation state is not just a simple function of P and T, but depends on phase assemblage, and may vary in a complex way within a single assemblage. The liquid model performs well, such that calculated solidus, melt productivity and liquid compositions compare favourably with those of experimental studies, permitting its use in interpolating between, and extrapolating from, experimental P–T conditions. Experimentally challenging but geologically useful regimes can be explored, such as subsolidus samples and very low melt fractions, with application to both mantle xenoliths and the origin of basalt.

Key words: basalt; mantle; partial melting; peridotite; thermodynamics

INTRODUCTION

Much experimental effort has been expended in deducing the mineralogy of the upper mantle and its melting behaviour, with the principal aim of understanding the origin of basaltic melts, and the underlying mantle geodynamic processes and the evolution of the Earth. Thermodynamic approaches to modelling melting in the mantle have been less successful, although the MELTS (and pMELTS) program has been of great value in understanding the way in which melts are generated from mantle melting and then crystallized on subsequent segregation, rise and cooling (Ghiorso & Sack, 1995; Asimow & Ghiorso, 1998; Ghiorso *et al.*, 2002). The subsolidus relations in peridotite have yet to be modelled in detail for compositions that contain ferric iron, particularly with respect to the effects of this component on the spinel to garnet transition interval. We also re-evaluate the thermodynamic properties of Cr-bearing end-members and their effect on phase equilibria (see Klemme, 2004; Klemme *et al.*, 2009), particularly with respect to the effects of these elements on the spinel to garnet transition interval. In addition, there remains a need to model the initial melting of peridotite in the range 0–60 kbar such that the phase relations and melt compositions are predicted accurately enough to be useful for trace-element geochemical modelling of melting processes. Although Green *et al.* (2012*a*) and Green *et al.* (2012*b*) made progress on subsolidus relations and on melting in the simplified CMAS system, respectively, the results were limited in application to more complex natural systems. This study, which builds on the dataset of Holland & Powell (2011), explores a simple thermodynamic model that aims to shed light on some of these aspects of mantle subsolidus and melting behaviour. It is, however, preliminary in scope and application.

Table 1: Cr and Fe^{3+} end-members in cpx and opx

		M2	M1	T
opx:	cren	Mg	Cr	AlSi
	mess	Mg	Fe^{3+}	AlSi
cpx:	crdi	Ca	Cr	AlSi
	cess	Ca	Fe^{3+}	AlSi

MODEL

A simple thermodynamic model for pyroxenes and spinel in NCFMASOCr

Green *et al.* (2012*a*) presented a thermodynamic model for garnet, pyroxenes and spinel in the CMAS subsystem, providing reasonable fits to the available experimental data. Although the scope of this model was extended by Holland *et al.* (2013) into deep mantle conditions in the slightly larger NCFMAS system, ferric iron and chromium were not included and melting was not considered. The consequences of adding Fe^{3+} and Cr to peridotites and their constituent phases is examined here, particularly with respect to the effects on the spinel–garnet transition and on melting at depth. Addition of Fe^{3+} and Cr in garnet is done via the end-members andradite (andr, $Ca_3Fe_2Si_3O_{12}$) and knorringite (knor, $Mg_3Cr_2Si_3O_{12}$), both of which exist already in the dataset of Holland & Powell (2011). The mixing model for garnets is an extension of that used by Holland *et al.* (2013) arising from consideration of the properties of knorringite, skiagite and andradite. Mixing parameters are explained and given in the Appendix.

Ferric and chrome end-members are required for pyroxenes, and are formulated as in Table 1 (where the following abbreviations are used: cren, Cr-enstatite; mess, Mg-esseneite; crdi, Cr-diopside; cess, Ca-esseneite).

The thermodynamics of these end-members and their mixing properties are derived using the approach of Powell *et al.* (2014), and results are given in the Appendix. Without experimental constraints these end-members can only be approximated, with the goal being the ability to make calculations that are consistent with the small ranges in ferric iron and chromium observed in upper mantle peridotites. In this approach, the major unknowns are the reciprocal M2–M1 energies $W_{CaAlMgFe}{}^{3+}$, $W_{CaAlFeFe}{}^{3+}$, $W_{CaAlMgCr}$, $W_{CaAlFeCr}$ in both cpx and opx. These are known to have large negative values of around 25–50 kJ in garnet (e.g. Gudmundsson & Wood, 1995). However, in pyroxenes these are likely to be much less than half those values because garnets involve twice the formula size of pyroxene, and the disparity in size and shape between M1 and M2 in pyroxenes is much less than that between the X and Y sites in garnet. A value of –10 kJ was taken for these interactions, a value that provides close agreement with the location of the opx-out boundary in the peridotite experiments of Walter (1998). Using these values and the approach of Powell *et al.* (2014) a set of interaction energies among pyroxene end-members has been derived (see Appendix). The enthalpies for the cess, mess, crdi, and cren end-members were derived by consideration of the compositions of natural peridotite KLB-1, and were adjusted until their absolute values and partitioning for spinel peridotite at pressures just below garnet appearance for temperatures in the range 900–1200°C (Fig. 1) matched the natural compositions given by Canil *et al.* (1994). The cess end-member enthalpy and entropy were then adjusted so as to match the temperature-dependent partitioning of Fe^{3+} between garnet and cpx (Woodland, 2009, fig. 4) along a *P–T* path from 30 kbar and 900°C to 60 kbar and 1350°C. Making the enthalpy of cess more negative makes cpx more ferric and lowers ln $D_{Fe^{3+}}^{gt/cpx}$ in the Woodland (2009, fig. 4) plot at all temperatures. Making the enthalpy of mess more negative gives more ferric iron to opx but has little effect on the Woodland (2009, fig. 4) ln $D_{Fe^{3+}}^{gt/cpx}$ vs $1/T$ plot. Increasing ferric iron in both cpx and opx drives the opx-out boundary in Fig. 1 up *T* and *P*. Values that match the Woodland (2009) plot and the measured ferric contents of Canil *et al.* (1994) are accepted. The model parameters for pyroxenes are given in the Appendix.

Spinels are described in terms of the end-members spinel (sp, $MgAl_2O_4$), hercynite (hc, $FeAl_2O_4$), magnetite (mt, $FeFe^{3+}{}_2O_4$) and picrochromite (pcr, $MgCr_2O_4$). Spinel thermodynamics are complex, involving both cation and magnetic disordering. The model presented here incorporates the simple spinel model of Bryndzia & Wood (1990), in which spinels are considered as mixtures of the cations randomly distributed on all three cation sites in the structure. Bryndzia & Wood (1990) fitted this simplified model as a parameterization to their more complex model and have used it successfully in oxybarometry for mantle spinels. The Bryndzia & Wood (1990) model provides values for interaction energies as $W_{sp,hc} = 4$, $W_{sp,mt} = 56$, $W_{sp,pcr} = 39$, $W_{hc,mt} = 32$, $W_{hc,pcr} = 27$ and $W_{mt,pcr} = 36$ (all in kJ). At the lowest temperatures considered here the spinel model may approach its limits of applicability, although it does provide a reasonable, but slightly low temperature (700°C) for the top of the hercynite–magnetite solvus.

A simple thermodynamic model for melts

In previous studies (e.g. Holland & Powell, 2001) a simple melting model was presented in terms of end-members expressed on an eight-oxygen basis. This simple model worked well in hydrous haplogranitic systems, but was inadequate in more mafic compositions where the degree of polymerization is less extensive and so a more complex model was used by Green *et al.* (2012*b*) for the CMAS system. The main problem encountered in the study of Green *et al.* (2012*b*) was that the distribution of entropy in melts with variation in composition was difficult to model. This work simplifies the problem by (1) restricting the melts to basaltic compositions formed from partial melting of peridotite and (2) introducing a Temkin type of entropy model (i.e. the number of sites in a lattice depends upon composition).

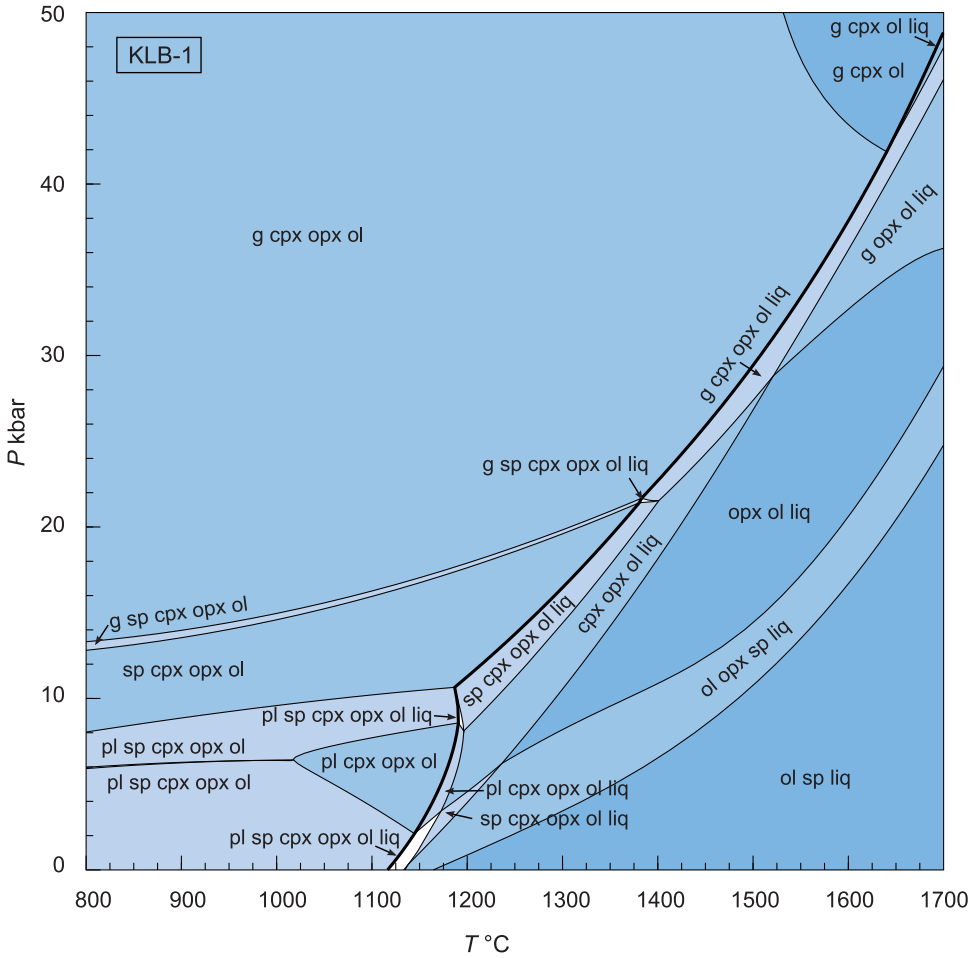

Fig. 1. *P–T* pseudosection calculated for KLB-1 in the NCFMASOCr system. Phases: g, garnet; sp, spinel; pl, plagioclase; ol, olivine; cpx, clinopyroxene; opx, orthopyroxene; liq, liquid. Lines denote phase boundaries; the bold line indicates the solidus (liq-out). Progressively darker fields indicate increasing variance, and thus decreasing number of phases. At subsolidus conditions, Cr-rich and Al-rich spinel are separated by a miscibility gap, where Cr-rich spinel occurs at lower pressures. At increasing temperatures, Al-rich spinel is lost in a melting assemblage, and reappears as Cr-rich spinel in low modal proportion (<0·01) in the high melt fraction assemblages (ol opx sp liq) and (ol sp liq), which may be an artefact of the simplified melt model.

It should be emphasized that the model presented here will not work for a wide range of compositions and involves pseudo-sites in the melt, which, as described below, are to be regarded as a useful preliminary device to model the melt entropy. Nevertheless, its success in describing the melting temperatures of peridotite and the compositions of melts produced at up to 60 kbar shows that it appears to work within the limits of its intended scope, and allows useful predictions to be made. This simple model for melt involves eight end-members ($jd = NaAlSi_2O_6$, $di = CaMgSi_2O_6$, $ct = CaAl_2SiO_6$, $fo = Mg_2SiO_4$, $fa = Fe_2SiO_4$, $q = Si_2O_4$, $ek = CrO_{1.5}$, $hm = FeO_{1.5}$) in a simple hypothetical structure composed of octahedral-like melt sites (M) set in a largely aluminosilicate framework (F) with additional larger sites (A). The end-members and their model structural elements are as shown in Table 2.

Random mixing of the seven species $AlSi_2$, Si_2^p, Al_2Si, Si, Si_2^q, Cr and Fe^{3+} on a network is assumed. The three types of Si units reflect the presence of chains (Si_2^p), isolated tetrahedra (Si) and three-dimensional network (Si_2^q) elements. Random mixing of Mg, Fe and Ca is assumed on separate M sites. The A sites are assumed to be occupied by Na and Ca from the jadeite and cats end-members. No mixing entropy is attributed to the A site under the assumption that Na is linked to neighbouring $AlSi_2$ triplets and Ca is linked to adjacent Al_2Si triplets to maintain local charge balance. Thus the activity terms below do not involve the A site. A Temkin-type model is assumed, where the number and occupancy of sites varies with melt composition. In terms of the M, F and A sites the numbers of species elements are as follows.

A sites:

$$Na = jd;\ Ca = ct$$
$$\sum A = jd + ct$$

M sites:

$$Mg = 2fo + di;\ Fe = 2fa;\ Ca = di$$
$$\sum M = 2fo + 2fa + 2di$$

Table 2: Melt end-members used in this study

	M	F	A
jd	—	$AlSi_2$	Na
di	CaMg	Si_2^p	—
ct	—	Al_2Si	Ca
fo	Mg_2	Si	—
fa	Fe_2	Si	—
q	—	Si_2^q	—
ek	—	Cr	—
hm	—	Fe^{3+}	—

Cations are allocated to M, F and A sites. (See text for details.)

F sites:

$$AlSi_2 = \text{jd};\ Al_2Si = \text{ct};\ Si_2^p = \text{di};\ Si = \text{fo} + \text{fa};$$
$$Si_2^q = \text{q};\ Cr = \text{ek};\ Fe^{3+} = \text{hm}$$
$$\sum \text{F} = 1 \cdot 0.$$

The ideal activities are then given by mixing on the various sites, in which Ca refers solely to that on the M site, as

$$a_{\text{jd}} = \frac{AlSi_2}{\Sigma F} = \text{jd}$$
$$a_{\text{di}} = 4\frac{Ca}{\Sigma M}\frac{Mg}{\Sigma M}\frac{Si_2^p}{\Sigma F} = 4\frac{\text{di}^2(\text{di}+2\text{fo})}{(2\text{fo}+2\text{fa}+2\text{di})^2}$$
$$a_{\text{ct}} = \frac{Al_2Si}{\Sigma F} = \text{ct}$$
$$a_{\text{fo}} = \frac{Mg^2}{(\Sigma M)^2}\frac{Si}{\Sigma F} = \frac{(\text{di}+2\text{fo})^2(\text{fo}+\text{fa})}{(2\text{fo}+2\text{fa}+2\text{di})^2}$$
$$a_{\text{fa}} = \frac{Fe^2}{(\Sigma M)^2}\frac{Si}{\Sigma F} = \frac{(2\text{fa})^2(\text{fo}+\text{fa})}{(2\text{fo}+2\text{fa}+2\text{di})^2}$$
$$a_{\text{q}} = \frac{Si_2^q}{\Sigma F} = \text{q}$$
$$a_{\text{ek}} = \frac{Cr}{\Sigma F} = \text{ek}$$
$$a_{\text{hm}} = \frac{Fe^{3+}}{\Sigma F} = \square\text{m}$$

and non-ideal terms come from a regular solution of the eight end-members (jd, di, ct, fo, fa, q, ek, hm). The model was developed in two stages. First, in the simpler NCFMAS system the end-member properties were taken directly from Holland & Powell (2011) and Holland *et al.* (2013). Next, approximate values were assigned to all of the interaction energies among the six end-members (omitting hm and ek), based on simple binary phase equilibria, where available [e.g. as described by Holland & Powell (2001) and Green *et al.* (2012*b*)]. Interaction energies between minor constituents in the melt have little or no effect and have been set to zero. This led to results that resembled, albeit imperfectly, the solidus temperatures and melt compositions for KLB-1 peridotite, so a Monte Carlo approach was undertaken to model the melting temperatures and melt compositions of KLB-1 peridotite to improve the Gibbs energy contribution of each end-member. As in the study by Holland & Powell (2001) only pressure dependences were allowed on the Gibbs energy corrections to end-members and the interaction energies among them, mainly to keep the number of adjustable parameters manageable. In the Monte Carlo simulations, filters were applied, both as temperature brackets for phase equilibrium features such as the solidus and for melt compositions expressed in terms of the end-member proportions. Specifically, the constraints imposed were as follows:

1. Beginning of melting of plagioclase peridotite at 1 bar, with a temperature bracket of 1120–1180°C (Takahashi *et al.*, 1993).
2. Beginning of melting at 30 kbar of garnet + olivine + clinopyroxene, with a bracket of 1480–1510°C (Takahashi *et al.*, 1993).
3. Beginning of melting of olivine + garnet + clinopyroxene at 46 kbar (1670–1710°C) and 65 kbar (1800–1840°C) from Takahashi *et al.* (1993).
4. The composition of the melt for (2) above was assumed to be that determined by Davis *et al.* (2011) for initial melt from KLB-1 at 30 kbar. In terms of end-member proportions the melt composition brackets used were ct (0·14–0·16), jd (0·14–0·16), di (0·19–0·21), fa (0·11–0·13), fo (0·25–0·27), with q making up the remainder, and not imposed.

The parameters that were varied were the end-member liquid enthalpies [via increments to values in the Holland & Powell (2011) dataset] and regular solution interaction energies (*W*) among them. Interaction energies were initially taken as known, and allowed to vary by 20% of their value to see if any adjustments were needed. Very little change was indicated, but this may be because the experimental constraints are much more sensitive to changes in the enthalpies of the end-member components. Some *W* values benefited from a small pressure dependence. Monte Carlo runs were made by successively imposing the constraints above until 500 successes at each stage were achieved through varying the set of parameters. The resulting model is therefore neither optimal nor unique, but is sufficient within the scope of the objectives in this clearly underdetermined system, and the Monte Carlo runs were performed mainly to check that the simple model parameters, based on minimal changes to the Holland & Powell (2011) dataset, were able to satisfy the applied constraints. Thermodynamic data for all end-members used here are presented in Table 3.

Addition of ferric iron and chromium to the system required estimation of free energies of the hm and ek end-members. The Holland & Powell (2011) dataset has been updated to include the two end-members hemL (Fe_2O_3) and eskL (Cr_2O_3) and derivation details are given in the Appendix. The hm ($FeO_{1.5}$) and ek ($CrO_{1.5}$) end-members used here are half the formula unit size of the dataset end-members. Application of these

Table 3: Thermodynamic data used in this study

	H	SD(*H*)	*S*	*V*	*a*	*b*	*c*	*d*	a_0	K_0	K'_0	K''_0
fo	–2172·45	0·53	95·10	4·366	0·2333	0·1494	–603·8	–1·8697	2·85	1285·0	3·84	–0·0030
fa	–1477·74	0·64	151·00	4·631	0·2011	1·7330	–1960·6	–0·9009	2·82	1256·0	4·68	–0·0037
py	–6281·77	0·99	269·50	11·313	0·6335	0	–5196·1	–4·3152	2·37	1743·0	4·05	–0·0023
alm	–5260·75	1·20	342·00	11·525	0·6773	0	–3772·7	–5·0440	2·12	1900·0	2·98	–0·0016
gr	–6643·05	1·37	255·00	12·535	0·6260	0	–5779·2	–4·0029	2·20	1720·0	5·53	–0·0032
andr	–5768·97	1·46	316·40	13·204	0·6386	0	–4955·1	–3·9892	2·86	1588·0	5·68	–0·0036
knor	–5707·56	2·65	302·00	11·738	0·6130	0·3606	–4178·0	–3·7294	2·37	1534·0	4·34	–0·0028
en	–3090·10	0·62	132·50	6·262	0·3562	–0·2990	–596·9	–3·1853	2·27	1059·0	8·65	–0·0082
fs	–2388·76	0·75	189·90	6·592	0·3987	–0·6579	1290·1	–4·0580	3·26	1010·0	4·08	–0·0040
mgts	–3196·60	0·69	131·00	6·050	0·3714	–0·4082	–398·4	–3·5471	2·17	1028·0	8·55	–0·0083
di	–3201·82	0·58	142·90	6·619	0·3145	0·0041	–2745·9	–2·0201	2·73	1192·0	5·19	–0·0044
hed	–2842·12	0·88	175·00	6·795	0·3402	0·0812	–1047·8	–2·6467	2·38	1192·0	3·97	–0·0033
jd	–3025·29	1·52	133·50	6·040	0·3194	0·3616	–1173·9	–2·4695	2·10	1281·0	3·81	–0·0030
acm	–2583·32	2·26	170·60	6·459	0·3071	1·6758	–1685·5	–2·1258	2·10	1060·0	4·08	–0·0038
kos	–2745·91	2·09	149·65	6·309	0·3092	0·5419	–664·6	–2·1766	1·94	1308·0	3·00	–0·0023
cats	–3310·11	0·75	135·00	6·356	0·3476	–0·6974	–1781·6	–2·7575	2·08	1192·0	5·19	–0·0044
ab	–3935·35	1·55	207·40	10·067	0·4520	–1·3364	–1275·9	–3·9536	2·36	541·0	5·91	–0·0109
an	–4232·62	0·75	200·50	10·079	0·3705	1·0010	–4339·1	–1·9606	1·41	860·0	4·09	–0·0048
esk	–1128·24	0·41	83·00	2·898	0·1190	0·9496	–1442·0	–0·0034	1·59	2450·0	3·60	–0·0015
sp	–2301·01	0·79	82·00	3·978	0·2229	0·6127	–1686·0	–1·5510	1·93	1922·0	4·04	–0·0021
herc	–1952·62	0·80	113·90	4·075	0·2167	0·5868	–2430·2	–1·1783	2·06	1922·0	4·04	–0·0021
mt	–1114·25	0·88	146·90	4·452	0·2625	–0·7205	–1926·2	–1·6557	3·71	1857·0	4·05	–0·0022
picr	–1760·31	2·44	118·30	4·356	0·1961	0·5398	–3126·0	–0·6169	1·80	1922·0	4·04	–0·0021
qL	–921·08	0·26	16·30	2·730	0·0825	0	0	0	0	220·0	9·46	–0·0430
foL	–2237·25	0·56	–62·00	4·312	0·2694	0	0	0	9·20	362·0	10·06	–0·0278
faL	–1462·85	0·66	96·00	4·677	0·2437	0	0	0	10·71	290·0	10·42	–0·0359
diL	–3193·84	0·66	42·10	7·288	0·3340	0	0	0	8·51	249·0	8·04	–0·0323
anL	–4277·90	0·79	29·00	10·014	0·4300	0	0	0	5·14	210·0	6·38	–0·0304
abL	–3926·39	1·56	149·90	10·858	0·3580	0	0	0	3·37	176·0	14·35	–0·0815
eskL	–1062·25	0·59	63·30	3·709	0·1576	0	0	0	7·03	150·0	6·00	0·0400
hemL	–875·14	0·74	–33·20	3·221	0·2290	0	0	0	19·53	230·0	4·00	–0·0174

H is the regressed enthalpy of formation from the elements at 1 bar and 298 K; SD(*H*) is one standard deviation on the enthalpy of formation; *S* is the entropy; *V* the volume (all properties at 1 bar and 298 K); *a*, *b*, *c* and *d* are the coefficients in the heat capacity polynomial $C_p = a + bT + cT^{-2} + dT^{-1/2}$; a_0 and K_0 are thermal expansion and bulk modulus at 298 K; K_0' and K_0'' are the first and second pressure derivatives of bulk modulus at 298 K. Units: *H*, kJ; *S*, J K^{-1}; *V*, kJ $kbar^{-1}$; C_p, kJ K^{-1}; a_0, T^{-1}; K_0, kbar. It should be noted that $C_p(b)$ and a_0 need to be multiplied by 10^{-5}. Further information on the dataset, including details of unchanged order–disorder parameters for ab, an, cats, sp, herc, mt and picr, has been given by Holland & Powell (2011). The complete updated thermodynamic dataset for use in calculations is provided in Supplementary Data. Data sources for end-members changed since Holland & Powell (2011) are as follows. esk: *V*, K_0 and K_0' from Kantor *et al.* (2012); *H* from Klemme & O'Neill (2000). alm: *S* and C_p from Dachs *et al.* (2012). knor: *S*, reduced after Wijbrans *et al.* (2014). eskL and hemL are discussed in text. Liquid end-member for cats (ct) derived from anL and qL (see Appendix). Liquid end-member for cats (jd) derived from abL and qL (see Appendix).

directly to the model did not result in acceptable melt compositions (especially for Cr). As the mixing properties are not known, the simplest procedure is to assume ideal interactions with all other melt end-members and to find increments to the free energies of hm and ek that reproduce what is known of the ferric and chrome contents of melts. Because the model allows calculation of the $Fe^{3+}/\Sigma Fe$ ratio of melts through the internal all-melt equilibrium $4\,hm + q = 2\,fa + O_2$ it was fitted to the calibrations of Kress & Carmichael (1991), Jayasuriya *et al.* (2004) and O'Neill *et al.* (2006). A very small enthalpy increment to hm leads to a very good fit to the experimental melts listed by Kress & Carmichael (1991) over a range in log fO_2 from –8·5 to –0·6 and temperatures from 1200 to 1630°C, and to agreement with the pressure dependence from O'Neill *et al.* (2006). In addition, use of the half formula size $FeO_{1·5}$ yields the correct log ($FeO_{1·5}$/FeO) vs log fO_2 slope of 0·25 as required (Jayasuriya *et al.*, 2004). It is remarkable that the melt model derived here required only one parameter to be adjusted (hm free energy changed by 0·2 *P* kJ) to fit the $Fe^{3+}/\Sigma Fe$ determinations over such large ranges of *P*, *T* and log fO_2. Graphical illustration of the fit to the Kress & Carmichael (1991) melt measurements is provided in the Supplementary Data (supplementary data are available for downloading at http://www.petrology.oxfordjournals.org). The resulting Fe_2O_3 and $Fe^{3+}/\Sigma Fe$ of a liquid calculated along the solidus of KLB-1 using this model are shown in Fig. 2. Whereas the hm end-member is well calibrated, the ek end-member is approximate and is based simply on matching the Cr contents of liquids at the solidus of KLB-1 using the data of Takahashi (1986) and Hirose & Kushiro (1993). The partitioning of Fe and Mg between olivine and melt was used to make small adjustments to the enthalpies of the foL and faL components to fit the relations seen as a function of pressure in the studies by Takahashi & Kushiro (1983) and Toplis (2005).

A final round of Monte Carlo runs was performed in the full NCFMASOCr system to estimate the approximate uncertainties on parameters. They are approximate because they are contingent on the assumptions built into the model. The model parameter values and uncertainties are given in the Appendix. The small size

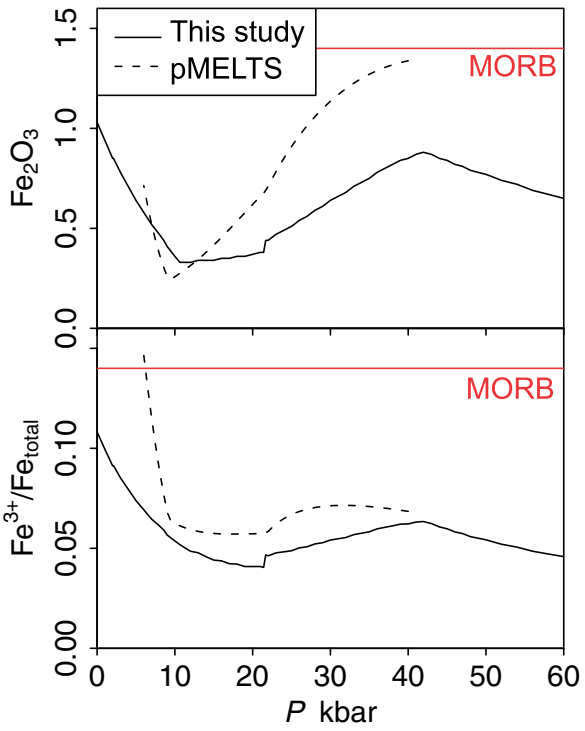

Fig. 2. Calculated $Fe^{3+}/\Sigma Fe$ and Fe_2O_3 of a nominal zero melt fraction (F) plotted against pressure along the KLB-1 solidus; continuous line, this study, dashed line, calculated in pMELTS. The red lines indicate that Fe_2O_3 and $Fe^{3+}/\Sigma Fe$ determined by Cottrell & Kelley (2011) for average primary MORB are somewhat higher than the calculated values for initial melts in this study. MORB is produced by polybaric, fractional and high fraction melting and so is not directly comparable with the isobaric isothermal $F = 0$ melts calculated here.

of the enthalpy increments (the Δ_i values in the Appendix) for all end-members supports the model assumptions made. Only the jd and ek liquid components required large Δ_i, but as the jd properties are derived from those of quartz and albite liquid this is not unexpected, and the ek end-member is derived from an estimated entropy of melting. The generally small (less than 10 kJ) Δ_i increments suggest that the entropy assumptions in the Temkin model are reasonable. A goal of this study is to provide a thermodynamic exploratory tool based on minimal assumptions, rather than an optimum melting model for peridotite, which must await a more refined study, closer agreement among experimental determinations and better understanding of the mixing properties in the melt. For example, there are significant differences in the experimental conditions determined for beginning of melting (e.g. Takahashi *et al.*, 1993; Walter, 1998; Davis *et al.*, 2011).

APPLICATION TO PERIDOTITES

The following examples take the bulk composition of KLB-1 as representative of fertile upper mantle peridotite. The bulk composition for KLB-1 is that of Davis *et al.* (2009) with 0·3 wt % Fe_2O_3 ($Fe^{3+}/\Sigma Fe = 0{\cdot}033$) and the appropriate correction to FeO to allow for this. The value of 0·3 wt % Fe_2O_3 was chosen on the basis of peridotite xenolith data presented by Canil *et al.* (1994), who reported values in the range 0·1–0·4 wt %. Most of the following discussion concerns the phase diagram for mantle peridotite calculated for the KLB-1 composition (Fig. 1). When other bulk compositions KR4003 and MM-3 are considered, the respective compositions given by Walter (1998) and Falloon *et al.* (2008) are used, with ferric iron set to 0·3 wt % Fe_2O_3. Calculations are performed using the program THERMOCALC (Powell *et al.*, 1998).

The implications of our model on subsolidus relationships, including the effect of Cr and Fe^{3+} on the depth and width of the spinel to garnet lherzolite boundary, as well as orthopyroxene stability, are investigated. This is followed by an investigation of the validity of the liquid model and some implications for mantle melting processes, before finally examining the calculated mantle oxygen fugacity as a function of pressure, temperature, mineral assemblage and bulk oxygen content.

Calculations for the same bulk compositions are also performed in pMELTS (Ghiorso *et al.*, 2002) using the alphaMELTS software (Smith & Asimow, 2005) with details of all pMELTS calculations provided in the Supplementary Data, in MAGPOX (Longhi, 1991) using the SPICEs MATLAB version (Davenport *et al.*, 2014), and using the melt composition parameterization of Till *et al.* (2012) and Grove *et al.* (2013) for comparison.

Subsolidus relationships

Pressure of the spinel to garnet transition

There is still much controversy over the experimental determination of the spinel to garnet transition (e.g. Jenkins & Newton, 1979; Gasparik, 1984; Robinson & Wood, 1998; Klemme & O'Neill, 2000; and discussion by Green *et al.*, 2012*a*). In Fig. 1 it may be seen that the pressure for this transition is somewhat lower than the values of some experiments on natural samples (e.g. Robinson & Wood, 1998; Walter, 1998). A simple argument is presented below to suggest that several experimental determinations have overestimated this transition pressure.

In the simple MAS subsystem there is fair agreement on the position of the transition among investigators; however, when Ca enters the system, the principal phase to admit Ca is garnet, which causes the pressure of the transition to drop because of the large effect of the drop in pyrope activity in the equilibrium

$$\mathrm{py} + \mathrm{fo} = 2\,\mathrm{en} + \mathrm{sp}.$$

In the CMAS system the reaction remains univariant (cpx joins the assemblage), but in more complex systems the variance becomes progressively larger and the reaction becomes a transition interval of finite width in pressure. Even in CMAS there is much disagreement over the pressure [see the discussion of Green *et al.* (2012*a*)], with some experimentalists favouring pressures as high as (or even higher than) that of the MAS reaction at high temperatures, which would be a

thermodynamic contradiction (Green *et al.*, 2012*a*). Calculations in this study favour the lower pressures and this is supported by a simple activity correction applied to the MAS reaction above, in which the compositions in MAS and CMAS are used along with activity models for garnet and opx. At 1480°C the MAS reaction (opx: $X_{AlM1} = 0{\cdot}20$) occurs at around 27·6 kbar (Gasparik & Newton, 1984). The pressure P for the CMAS (or other) assemblage of known ln K at temperature T is given by

$$P = P_{MAS} + \frac{RT}{\Delta V}(\ln K_{MAS} - \ln K).$$

In the expression above, P_{MAS} is the pressure of the MAS reaction, R is the gas constant, T is the temperature in Kelvin, and ln K_{MAS} and ln K are the equilibrium constants for the MAS reaction and for the larger system; ΔV (0·681 J bar^{-1}) is the volume change for the MAS reaction at these P–T conditions from Holland & Powell (2011).

The activity correction for the measured CMAS compositions (gt: $py_{86{\cdot}5}gr_{13{\cdot}5}$; opx: $X_{MgM2} = 0{\cdot}91$; $X_{AlM1} = 0{\cdot}20$; Green *et al.* 2012*a*), using the equation above, gives a pressure of 23·5 kbar, in close agreement with the Holland & Powell (2011) dataset calculations. Applying the same logic to the measured compositions given by Robinson & Wood (1998) at 1480°C, where they found a rather small pressure interval for the transition, activities of pyrope, enstatite, spinel and forsterite at 1480°C (using the activity models outlined above and in the Appendix, although ideal mixing yields almost the same change) result in a pressure drop of 4·8 kbar relative to the published value, giving a pressure of 22·8 kbar for the transition. This is almost identical to the pressures illustrated for the natural peridotite KLB-1 in Fig. 1, which is unsurprising as the dataset uses the MAS reaction experiments in its calibration. These calculations are taken to suggest that the lower pressure determinations of the transition in CMAS and hence natural compositions are correct. There is clearly an unresolved pressure calibration discrepancy remaining among the published experiments. The only alternative would be to imply that the MAS reaction and a huge number of other experimentally determined equilibria involving MAS minerals are at rather different pressures than currently accepted.

Effect of Fe^{3+} and Cr on the spinel to garnet transition

Figure 1 shows the calculated position of the spinel–garnet transition for this bulk composition. The transition interval is much less than 1 kbar wide at 800°C and narrows to about half that at the solidus. The effects of variable Fe^{3+} and Cr on this transition in terms of position and width are shown in the P–X pseudosections at 1100°C and 1400°C (Fig. 3). At 1100°C (Fig. 3a and b) the spinel–garnet field is extremely narrow at the composition of KLB-1, but widens significantly as the amount of these elements increase. The pressure at which garnet appears is almost independent of Cr content (Fig. 3a), whereas garnet-in moves to higher pressures with increasing Fe^{3+} content (Fig. 3b). The spinel-out boundary is sensitive to both increasing Cr and Fe^{3+}, with the transition becoming over 10 kbar wide at high Cr contents (Fig. 3a).

At 1400°C the spinel–garnet transition is of negligible width for the published Cr content of KLB-1 but it widens to higher values with increasing Cr (Fig. 3c). Increasing Fe^{3+} contents move the transition zone to higher pressures, as at 1100°C, but the zone remains rather narrow at all Fe^{3+} contents (Fig. 3d). Through thermodynamic analysis of experiments in the MASCr system, Klemme (2004) predicted a similar widening of the transition zone with increased Cr content, caused predominantly by the increasing stability of spinel at higher pressures.

The pMELTS model shows a stronger effect of bulk Cr_2O_3 on garnet-in than this study (see also Smith & Asimow, 2005): for the KLB-1 bulk composition, pMELTS matches the calculated garnet-in pressure well (21·5–22 kbar on the solidus), whereas for a doubled Cr_2O_3 content, the boundary shifts to 24–24·5 kbar. pMELTS predicts spinel stability over a far wider pressure range for KLB-1 than this study, reflecting the absence of any host other than spinel for Cr_2O_3 in the pMELTS model (P. D. Asimow, personal communication, 2015).

Chromium in spinel

The P–T pseudosection in Fig. 4a shows that the Cr content in spinel is highly pressure sensitive when plagioclase is present in the assemblage and highly insensitive when plagioclase is absent, indicating its potential as a low-pressure barometer for plagioclase–spinel lherzolites. The convergence of XCr isopleths at 6 kbar highlights the presence of a miscibility gap between Cr-rich spinel at low pressure and Cr-poor spinel at high pressure, also shown in Fig. 1, although at this pressure the spinel mode is very low.

Aluminium in orthopyroxene

Figure 4b shows calculated isopleths for Al in orthopyroxene in the garnet, spinel, and plagioclase fields for the KLB-1 composition. Isopleths are very steep in the spinel field and have modest positive slopes in the garnet field, as is well known from experimental studies (e.g. Perkins & Newton, 1980). More surprising is the flat negative slope of the isopleths in the plagioclase field [as noted earlier by Gasparik (1984)], providing a potential barometer for low-pressure peridotites. However, it is important to note that these isopleths are affected by the amounts of Fe^{3+} and Cr in the pyroxene M1 sites.

Although Fig. 4b is not a general Al-in-opx barometer, it may be used with caution for rocks very close in bulk composition to KLB-1. As an example, sample 313-106 from Vitim (Siberia) has a bulk composition close to KLB-1 (Ionov, 2004) and contains orthopyroxene with

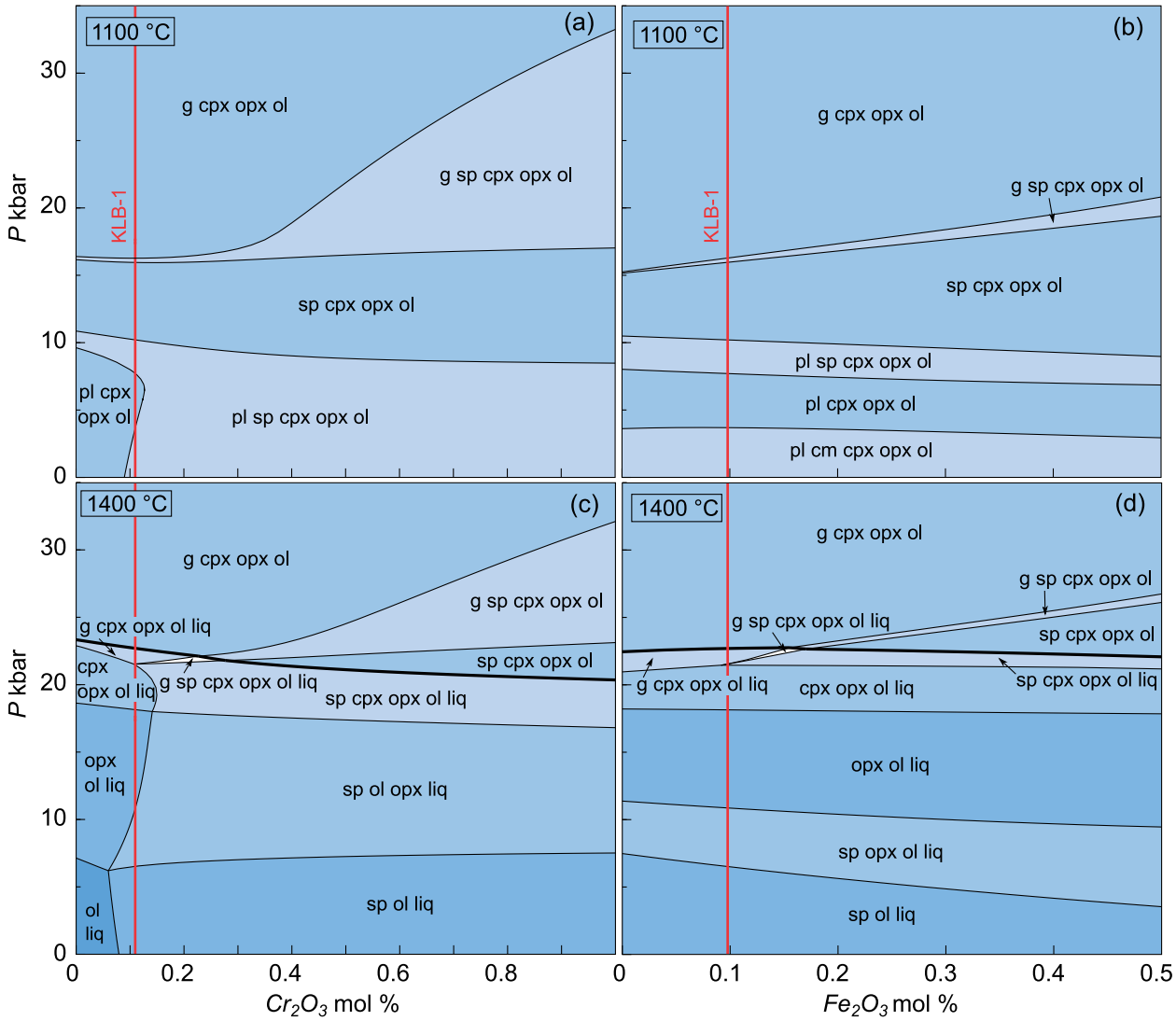

Fig. 3. *P–X* pseudosections for KLB-1 showing the effect of varying the molar proportions of Cr_2O_3 and Fe_2O_3 in the bulk composition on phase equilibria in isothermal sections. Red lines indicate the molar proportion of the oxide in the KLB-1 composition. Bold black lines are the solidus; phase labels as in Fig. 1. (a) Cr_2O_3, 1100°C; (b) Fe_2O_3, 1100°C; (c) Cr_2O_3, 1400°C; (d) Fe_2O_3, 1400°C. Both oxides have the effect of stabilizing spinel at higher pressures. It should be noted that the *x*-axis range in (b) and (d) is half that of (a) and (c).

0·18Al on a six-oxygen formula basis. Assuming that this is evenly divided between the T and M1 sites, a value of X_{AlM1} of 0·09 in Fig. 4b corresponds extremely closely to published barometry and thermometry of 21–23 kbar and 950–1050°C for the garnet peridotite samples (Ionov, 2004).

Disappearance of orthopyroxene at high temperatures

The pressure at which orthopyroxene disappears from the solidus in experimental studies is controversial (e.g. Takahashi, 1986; Herzberg *et al.*, 1990; Canil, 1992; Zhang & Herzberg, 1994; Walter, 1998). In Fig. 1 the calculated orthopyroxene-out boundary meets the solidus at 42 kbar and 1647°C, in good agreement with the experiments of Zhang & Herzberg (1994) and Walter (1998). The modal proportion of orthopyroxene in the KLB-1 composition is illustrated in Fig. 4c, where it decreases rapidly with increasing *P* and *T* in garnet-bearing assemblages. In a previous thermodynamic study (Holland *et al.*, 2013) it was shown that this boundary is highly sensitive to bulk composition, helping to explain the variation seen in experimental studies.

The highest modal proportions for opx occur in the spinel lherzolite field, decreasing up-pressure in the garnet field, and decreasing down-pressure in the plagioclase field.

Melting of peridotite

The onset and productivity of melting

The calculated solidus across the pressure range of Fig. 5a shows excellent agreement with experimental

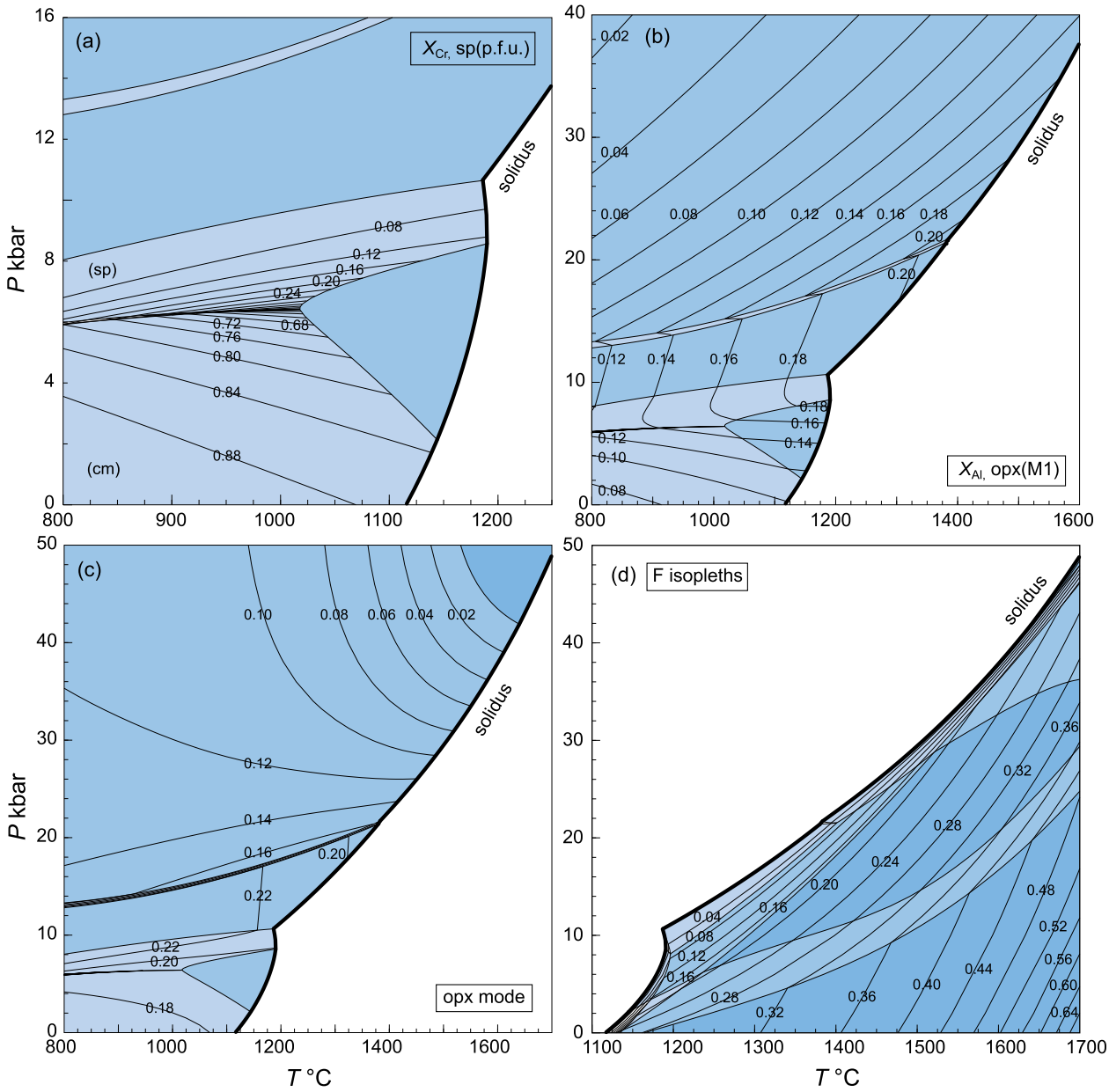

Fig. 4. Isopleths of constant modes or phase compositions in *P–T* space, calculated for KLB-1. Phase fields correspond to those in Fig. 1. (a) Molar proportion of Cr in spinel, per formula unit (p.f.u.). Two sets of isopleths appear to intersect at around 6 kbar, highlighting a miscibility gap where Cr-rich (cm) and Al-rich (sp) spinel compositions can coexist. (b) Molar proportion of Al in the opx M1 site. (c) Modal proportion of opx. (d) Modal proportion of liquid (melt fraction, *F*). It should be noted that the *x*- and *y*-axis ranges differ for each plot.

data and published parameterizations. This is to be expected, as the liquid model is calibrated so that the onset of melting is bracketed by the experiments of Takahashi *et al.* (1993). The cusp in the solidus of this study and the pMELTS calculation at 10 kbar is caused by an increased albite content of plagioclase, and therefore an increased fusibility of plagioclase just before the plagioclase-out pressure is reached; this geochemical feature was also observed experimentally by Borghini *et al.* (2010) and its effect on the solidus is also predicted by the pHMELTS model (e.g. Smith & Asimow, 2005).

Unlike the solidus temperature, the temperature of the liquidus (Fig. 5a) and that of intermediate melt fractions (Fig. 5b) are not used in the liquid model calibration. It is encouraging to see that both of these properties predicted by this model match published experimental parameterizations well. In particular, Fig. 5b shows a cusp in melt productivity at around 20% melt. This change in melt productivity is a result of cpx exhaustion (i.e. the lherzolite to harzburgite transition), and both the position of the cusp and the slope of the curve on either side match the parameterization of Katz *et al.* (2003) well. The fit is less good at high melt

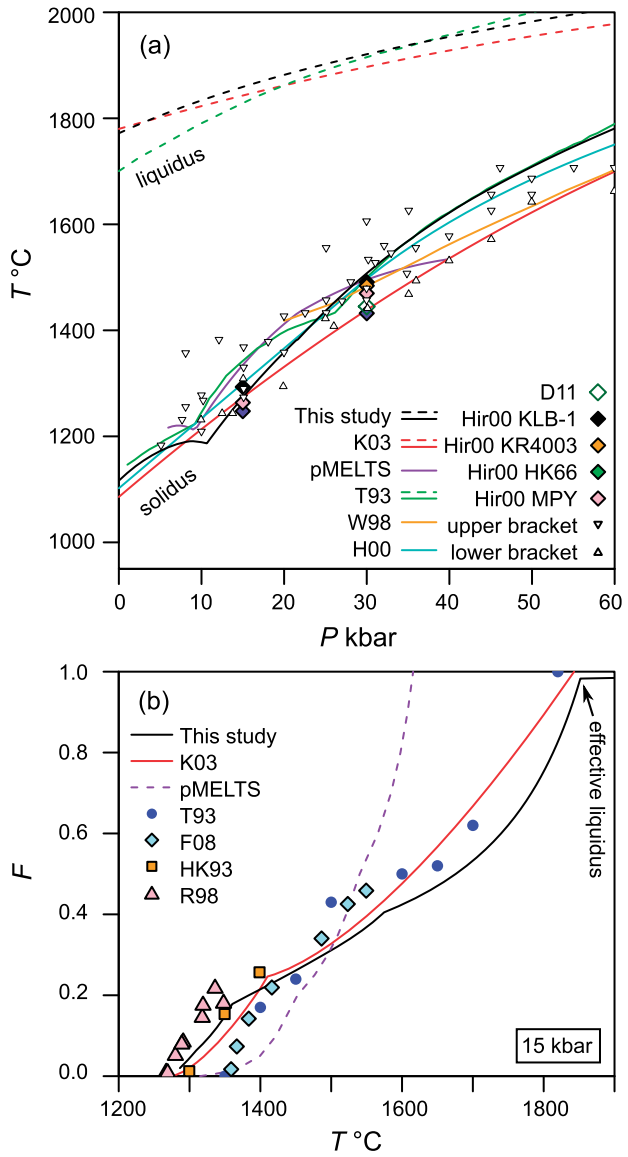

Fig. 5. (a) Solidus (continuous lines) and liquidus (dashed lines) pressure as a function of temperature, calculated in this study for KLB-1, with experimental data and other parameterizations plotted for comparison. Abbreviations: K03, Katz *et al.* (2003); pMELTS, KLB-1 in the system NCFMASOCrTi calculated in pMELTS; T93, KLB-1, Takahashi *et al.* (1993); W98, KR4003, Walter (1998); H00, KLB-1, Herzberg *et al.* (2000); D11, KLB-1, Davis *et al.* (2011). Hir00 indicates solidus position calculated by Hirschmann (2000) for given bulk compositions. Upper bracket and lower bracket are experimental data points that bracket the solidus position from the compilation of post-1988 experiments of Hirschmann (2000). There is good agreement between this study and others. (b) Isobaric melt fraction (F) as a function of temperature at 15 kbar calculated in this study for KLB-1 and shown with experimental data and other parameterizations for comparison. Additional abbreviations: F08, MM-3, Falloon *et al.* (2008) and references therein; HK93, KLB-1, Hirose & Kushiro (1993) recalculated by Hirschmann (2000); R98, MPY, Robinson *et al.* (1998). The cusp at around $F=0{\cdot}2$ seen in the three lines (this study, K03 and pMELTS) is caused by the exhaustion of clinopyroxene. 'Effective liquidus' is the olivine-out boundary in this study, beyond which a small mode (<1%) of spinel persists to high temperatures; this behaviour is probably a model artefact.

fractions. At 1750°C, the melt fraction predicted in this study is 0·16 lower than that predicted by Katz *et al.* (2003), and looks lower than that expected by interpolating between the experimental observations of Takahashi *et al.* (1993). This is a result of the higher liquidus temperature in this study, which in turn may reflect the lack of K_2O and volatile phases in our system, which is not the case for natural samples. There is also a lack of experimental observations, and thus understanding of melt productivity, at high melt fractions. High melt fractions have little relevance to current mantle melting processes, although they are important when considering magma ocean crystallization and Archaean mantle melting. The 'effective liquidus' of Fig. 5b is the point at which olivine is lost from the assemblage; a small fraction (<1%) of spinel persists in the melt to higher temperatures, indicating a possible model shortcoming at liquidus temperatures.

It can be seen in Fig. 4d that melt isopleths are compressed at higher pressure; that is, higher melt fractions are reached over a smaller temperature increase. This feature is also predicted in the Katz *et al.* (2003) model. Greater melt productivity at higher pressures in the mantle reduces the requirement for fusible recycled material to be present to account for excess crustal thickness observed at the surface at hotspots (cf. Foulger & Anderson, 2005).

Mineral modes and melt reactions along the solidus

Mineral modes calculated along the solidus for KLB-1 are shown in Fig. 6. They are in good agreement with experimental data for lherzolite; modes at the KLB-1 solidus at 30 kbar determined by Davis *et al.* (2011) are shown for comparison. There is general agreement with the pMELTS model, except in the pyroxenes and in the persistence of spinel to high pressure (Fig. 6; see also Smith & Asimow, 2005). The garnet–spinel transition occurs over a narrow pressure range, with the two phases coexisting at the solidus at 21·4–21·7 kbar; its position and the width are sensitive to bulk Cr_2O_3 and Fe_2O_3 (see above discussion). It can also be seen in Fig. 6 that the spinel to garnet transition consumes significant opx and some cpx, and precipitates some olivine. Orthopyroxene mode decreases with pressure along the solidus, disappearing completely at 42 kbar. At elevated mantle potential temperature T_p, where the adiabat intersects the solidus at greater than 42 kbar, the melting assemblage would be opx-free.

A good constraint on both mineral mode and melting reaction at the onset of melting is particularly important for trace element modelling. Melting reaction coefficients for KLB-1 at the solidus, calculated over a 0–1% melt fraction (or until a phase is exhausted, whichever comes first), are shown in Fig. 7. Opx is precipitated during melting at pressures above 5 kbar until it vanishes from the solidus, at which point it precipitates only after a threshold melt fraction is reached. Olivine is precipitated during spinel lherzolite melting and is

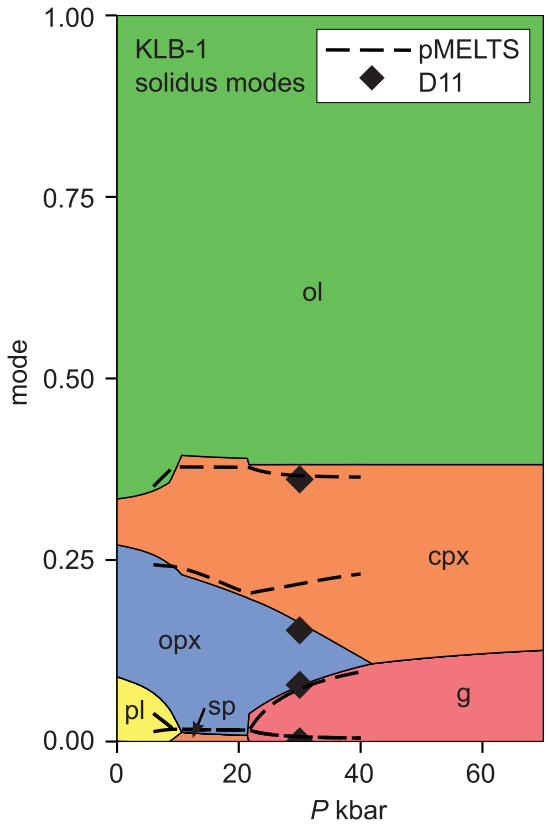

Fig. 6. A modebox diagram for KLB-1 bulk composition at pressures along the solidus, showing modal phase proportions (normalized molar) as a function of pressure. Phase labels as for Fig. 1. Although Fig. 1 indicates the presence of Cr-rich spinel on the solidus at 0–2·2 kbar, it can be seen here that its modal proportion is negligible. Diamonds show experimentally determined modes at 30 kbar on the KLB-1 solidus from Davis *et al.* (2011) (D11). Dashed lines are the same mode boundaries calculated along the solidus of KLB-1 in pMELTS in the system NCFMASOCrTi, which are in general agreement with the model presented here, except for the cpx:opx ratio in garnet-bearing assemblages.

consumed at higher pressures. Experimentally determined melting reactions are shown for comparison, although it should be noted that these are determined for bulk compositions MM-3 and KR4003. Although the sign of the reacting phase is usually in agreement with experimental values [in the experiments of Walter (1998), opx is consumed, olivine is precipitated and the direction of the pressure dependences matches those of this study] the coefficient is often different. This reflects a combination of experimental uncertainty, including phase proportion determinations, model shortcoming, and the different melt fractions over which the reactions are calculated.

Melt composition

Mantle melting is fractional, whereas this study of the behaviour of KLB-1 is relevant for an equilibrium system. The nominal 0% melt fraction composition, however, is important to model well, as it also represents the composition of melts at the onset of melting for fractional melting of the mantle. If these melt compositions also hold true at somewhat more depleted bulk

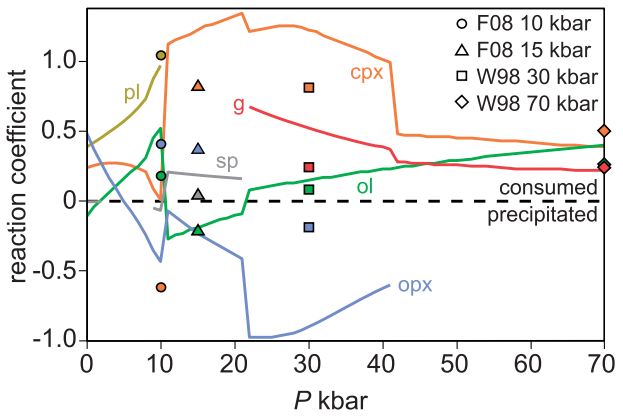

Fig. 7. Melt reaction coefficients for near-solidus melting plotted against pressure, calculated for KLB-1. Reaction coefficients are given such that negative values correspond to phase precipitation and liq = –1 in all instances. Reactions are calculated over the melt fraction range 0–0·01. Selected experimentally derived values are shown for comparison: W98 (Walter, 1998, KR4003) and F08 (Falloon *et al.*, 2008, MM-3, plagioclase lherzolite reaction only is shown at 10 kbar), although it should be noted that these were determined on slightly different bulk compositions.

compositions, this melting model can effectively be used to model a realistic fractional melting scenario.

With this in mind, the model 0% melt fraction composition for KLB-1 is compared with those determined experimentally by Falloon *et al.* (2008) for MM-3, and Herzberg & Zhang (1996) and Davis *et al.* (2011) for KLB-1 (Fig. 8a). Falloon *et al.* (2008) and Davis *et al.* (2011) employed iterative techniques to constrain the putative melt composition, whereas Herzberg & Zhang (1996) made use of the experimental temperature gradient and applied crystal/liquid partition coefficients in conjunction with an assumed SiO_2 content to calculate the liquid composition. The 30 kbar composition of Davis *et al.* (2011) was, in part, used in the model calibration. Even so, the fit to all points in Fig. 8a is very good, and demonstrates the effectiveness of the model in interpolating between the fixed *P*–*T* conditions of single experiments, making them applicable to a wide range of mantle *P*–*T* conditions. For comparison, Fig. 8b and c shows the predicted KLB-1 solidus liquid composition of pMELTS, Till *et al.* (2012) and Grove *et al.* (2013); pMELTS does not predict this very low melt fraction well, particularly in terms of CaO and at high pressure. The Till *et al.* (2012) and Grove *et al* (2013) parameterizations do a very good job, although to calculate these compositions, Mg# and NaK# were required from the THERMOCALC output, so the good fit is not entirely independently predicted.

Noteworthy features of Fig. 8 include the cusps in compositions at 10 kbar (at the plagioclase–spinel transition), and the Na_2O content of the melt, which decreases with increasing pressure [the uncertainty on the 50 kbar melt Na_2O of Herzberg & Zhang (1996) is very large]. Changes in Na_2O can be described by a pressure-dependent effective bulk partition coefficient (D_{Na}^{bulk}). The only solid phases in the presented

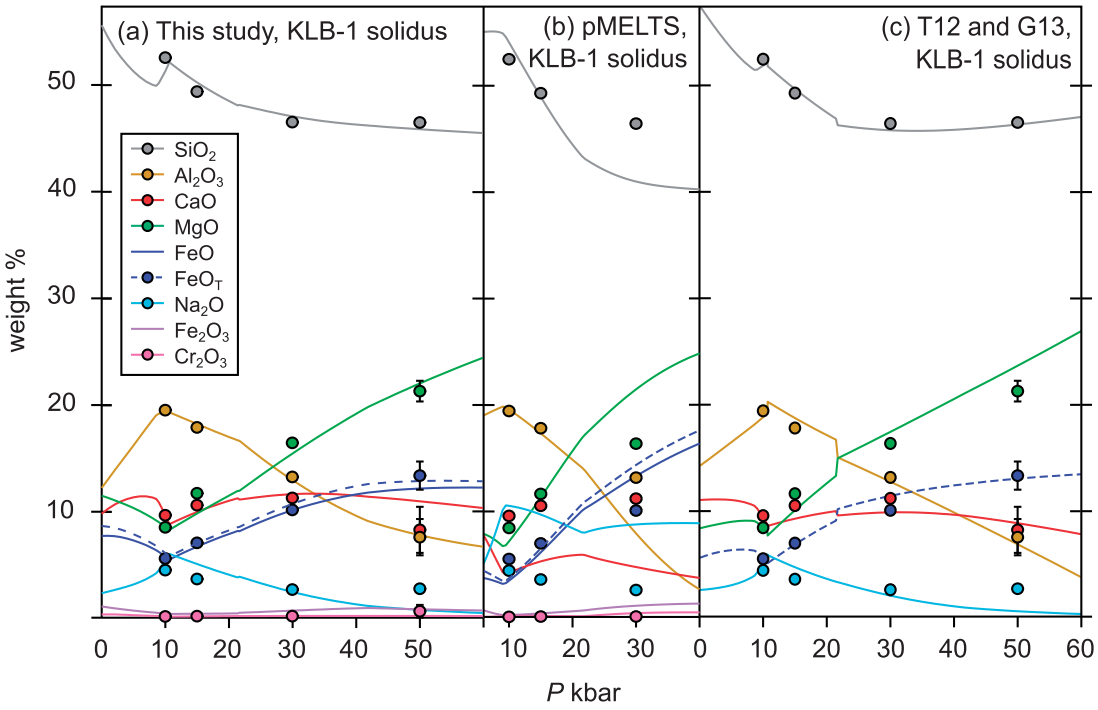

Fig. 8. Calculated composition (in wt % oxide) of melts of KLB-1 along the solidus (i.e. for a nominal zero melt mole fraction) as a function of pressure. Filled circles are experimental zero melt fraction compositions: 10 and 15 kbar points from bulk composition MM-3, Falloon *et al.* (2008) and references therein; 30 kbar points from KLB-1, Davis *et al.* (2011), error bars smaller than symbol; 50 kbar points from KLB-1, Herzberg & Zhang (1996), published uncertainties shown, except for Na_2O, which has a high uncertainty. FeO_T denotes total Fe reported as FeO. Experimental Fe is given as FeO_T only, as $Fe^{3+}/\Sigma Fe$ is unknown. For ease of comparison, model results in (a) and (b) are both (1) given as FeO and Fe_2O_3 individually (continuous lines) and (2) recalculated as FeO_T (dashed line). (a) KLB-1 bulk composition, melts at $F=0$, this study. MM-3 and KLB-1 have similar compositions, resulting in a good model fit to both. (b) KLB-1 bulk composition in NCFCMASOCrTi, melts at $F=0{\cdot}005$, calculated in pMELTS. (c) T12 (Till *et al.*, 2012, plagioclase and spinel lherzolite models for $P<20{\cdot}7$ kbar) and G13 (Grove *et al.*, 2013, garnet lherzolite model for $P>20{\cdot}7$ kbar). Steps in the curves result from three models being used for the different lithologies, where the compositions at phase boundaries from two models do not perfectly match. For the calculation, some melt chemical components must be known, such as Mg#, NaK#, K_2O, TiO_2 or P_2O_5. Mg# and NaK# are taken from the present model output at $F=0$ [i.e. (a)]; $K_2O=0{\cdot}01$, $TiO_2=0{\cdot}85$ and $P_2O_5=0$. For this reason, the good fit in some elements is a result of combining the model of this study with T12 and G13 and is not independently predicted.

simplified model that include Na-bearing end-members are plagioclase and cpx (see Appendix); therefore, above 10 kbar, cpx is the sole phase controlling melt Na_2O. It follows that D_{Na}^{cpx} must increase with increasing pressure, as proposed by Blundy *et al.* (1995). Figure 9 shows the calculated bulk/liquid and cpx/liquid D_{Na} of this study, that of Blundy *et al.* (1995) and that of pMELTS, all calculated along the solidus of KLB-1. It is seen that the pressure dependence of both parameters in the present model is similar to that of Blundy *et al.* (1995), with both showing similar absolute values and a similar pressure dependence up to around 40 kbar, where they diverge. The pMELTS model has a weaker pressure dependence. The pressure dependence of D_{Na}^{cpx} in the present model results in melts with the highest alkali/silica ratio being produced at moderately low pressures and low melt fractions, specifically around the plagioclase–spinel transition (10 kbar). Understanding Na partitioning in peridotite is vital for investigating the origin of alkali basalts.

The liquid model can be tested further by examining the compositions of higher fraction melts in relation to experimental studies. Figure 10a shows isobaric melt composition (15 kbar) calculated at a range of temperatures (i.e. melt fraction *F*), for bulk composition MM-3. This involves a spinel-lherzolite solidus assemblage and is directly comparable with the study of Falloon *et al.* (2008). A good fit to the data is observed. Major inflections are caused by the exhaustion of cpx at around $F=0{\cdot}22$. The equivalent of Fig. 10a with calculations performed using pMELTS rather than the present model, also on MM-3 at 15 kbar, is shown in Fig. 10b for comparison. The fit to experiments is also close, except in MgO. At very low melt fraction, the fit deteriorates, as is also indicated by Fig. 8b. At 30 kbar (Fig. 10c; garnet-lherzolite solidus assemblage), model melt composition at a range of melt fractions calculated for the bulk composition KR4003 is compared with those of Walter (1998). The fit is less close but still reasonable, more so at lower melt fractions, where the present model indicates perhaps a greater effect of cpx-out on the liquid composition. At low melt fraction, there is an offset between modelled and experimentally determined CaO in the melt.

In summary, the liquid compositions predicted by this simple model are in good agreement with

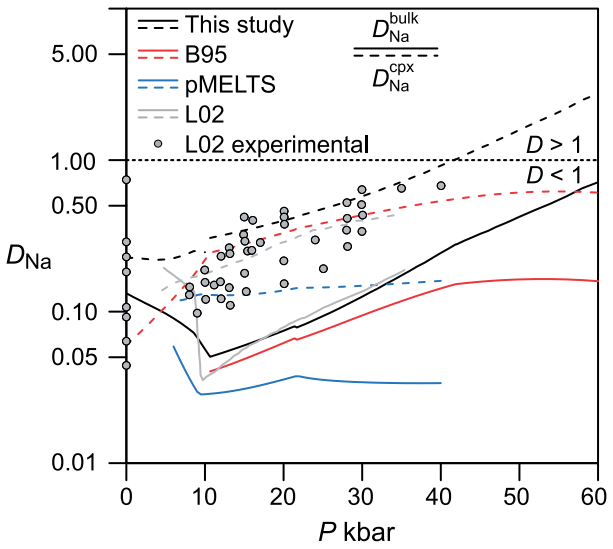

Fig. 9. Effective D^{cpx}_{Na} (dashed lines) and bulk D^{bulk}_{Na} (continuous lines) as a function of pressure along the solidus of KLB-1. Calculations are performed on KLB-1 for this study. Below 10 kbar, bulk D^{bulk}_{Na} is controlled by both plagioclase and cpx. B95; Blundy *et al.* (1995): D^{cpx}_{Na} calculated using *P* and *T* of the KLB-1 solidus calculated by the present model. Bulk D^{bulk}_{Na} was calculated using modelled modal proportion of cpx from KLB-1 along the solidus, assuming Na is incompatible in all other phases. Above 40 kbar, the two models diverge and Na becomes compatible ($D > 1$) in cpx in the model of this study, but not in B95. Shown for comparison are the pMELTS solution along the KLB-1 solidus, and L02, the calculated values for DPUM $F = 0{\cdot}01$ of Longhi (2002). Experimental data are a compilation of D^{cpx}_{Na} from L02.

experimentally produced liquids. The model is effective at low melt fractions, making it valuable for exploring fractional melting of the mantle, with application to the origin of basalt.

Olivine–liquid Fe–Mg partitioning along the solidus

$K^{ol-liq}_{D\,Fe-Mg}$ was defined by Roeder & Emslie (1970) to characterize Fe–Mg exchange between olivine and liquid. Recent experiments and an evaluation of published data place the 1 atm $K^{ol-liq}_{D\,Fe-Mg}$ at 0·34 for tholeiitic compositions (Matzen *et al.*, 2011), although the *P*–*T* dependence of this parameter is much less well constrained.

Figure 11 shows the $K^{ol-liq}_{D\,Fe-Mg}$ of this model for KLB-1 calculated at the solidus (i.e. for a 0% melt fraction) and at a 12% melt fraction. Single experimental data points and published composition-dependent parameterizations (using calculated melt compositions) are shown for comparison. At the plagioclase-out boundary around 10 kbar, the solidus melt reaches an unusual composition (Fig. 8). The high Na_2O and Al_2O_3 in the melt affects $K^{ol-liq}_{D\,Fe-Mg}$, albeit in an opposite sense to the published parameterizations of Herzberg & O'Hara (2002) and Toplis (2005). The resulting cusps in the $K^{ol-liq}_{D\,Fe-Mg}$–*P* relationship vanish at higher melt fractions, where melt compositions vary more smoothly. The 10 kbar 0% melt is Na- and Al-rich and Mg-poor, and may not be represented in the calibration range of these studies.

At pressures below 40 kbar, the melt model agrees with experimental data and published parameterizations. Above this, the model $K^{ol-liq}_{D\,Fe-Mg}$ values appear somewhat high, especially given that experimental evidence indicates $K^{ol-liq}_{D\,Fe-Mg}$ reaching a plateau (Herzberg & Zhang, 1996; Taura *et al.*, 1998) or even reducing (Mibe *et al.*, 2006) at higher pressures of up to 150 kbar.

Oxidation state

Determination of oxidation state entails measurement of Fe^{3+} in minerals, particularly garnet and spinel. In Fig. 12 calculated Fe^{3+} contents of garnet, cpx and opx are plotted as a function of *P* and *T*. Cpx Fe^{3+} contents fall with rising temperature [as noted by Woodland (2009)] and decreasing pressure in the garnet field but remain essentially constant in the garnet-absent field. Isopleths of opx Fe^{3+} content are shallower and thus more *P*-sensitive than in cpx, and result in the highest opx Fe^{3+} content occurring at high temperature and low pressure in garnet lherzolites, matching the observation of Nimis *et al.* (2015) on natural mantle xenoliths. Garnet Fe^{3+} increases strongly with pressure, and to a lesser extent with temperature. This results in a decreasing $D^{opx/g}_{Fe^{3+}}$ with increasing *P* along a geotherm, also in agreement with Nimis *et al.* (2015). The often-quoted increase in Fe^{3+} in garnet with temperature (e.g. Canil & O'Neill, 1996; Woodland & Peltonen, 1999; Woodland & Koch, 2003) is deceptive, as pressure is the more important variable, and it occurs because the xenolith suites studied lie on geotherms where higher temperatures are reached at higher pressures in the mantle. In the melt region in Fig. 12, isopleths of the hm end-member $FeO_{1{\cdot}5}$ in the liquid are plotted, and their profile along the solidus (in units of wt % Fe_2O_3) is also shown in Fig. 2. The trend of changing ferric iron content of the melt with changing *P*–*T* condition changes as a function of assemblage, particularly across the plagioclase-out and opx-out boundaries. These calculations refer to a mantle assemblage whose log fO_2 is not fixed by any oxygen buffer, and other redox equilibria involving C, H, S, Mn, V, etc. are not considered.

Values for log fO_2 relative to the quartz–fayalite–magnetite (QFM) buffer calculated over a range of pressures and temperatures are shown in Fig. 13. The left-hand plot shows a log fO_2 profile along three isothermal slices and the solidus. The most striking observation is the dominating effect of mineral assemblage on mantle log fO_2. A log fO_2 'trough' is observed near the spinel lherzolite solidus, and an interval is observed in the [g cpx opx ol] stability field at low pressure where log fO_2 briefly increases with pressure before decreasing. In the supersolidus, the opx-out boundary defines a change in trend of log fO_2 with *T*. The effect of both pressure and temperature on log fO_2 is complex.

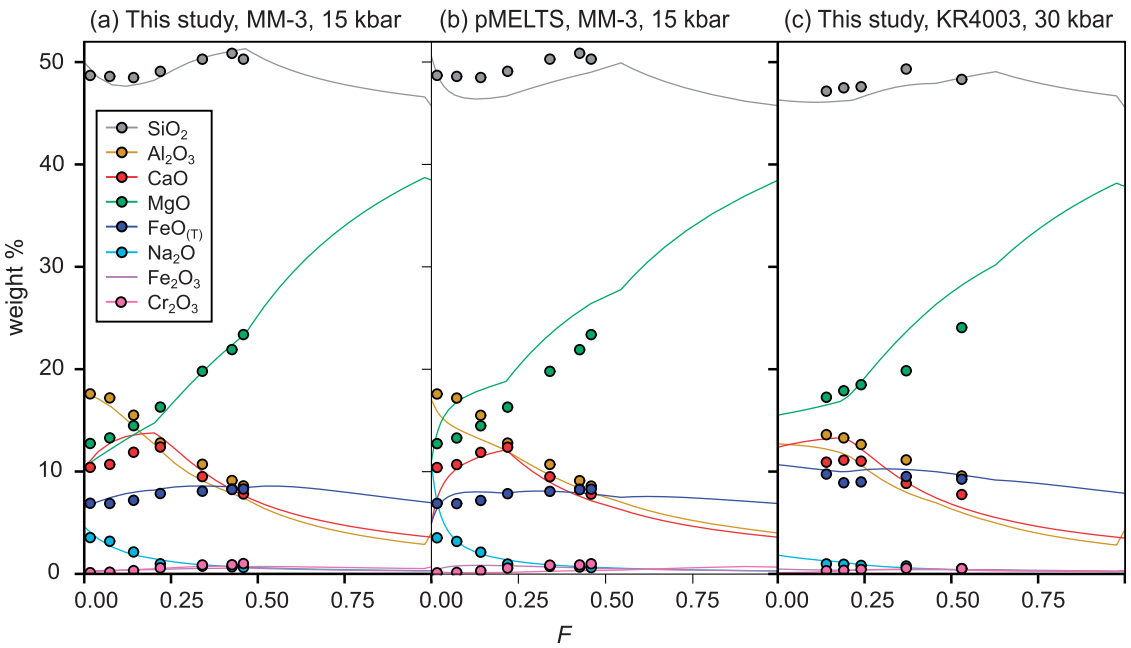

Fig. 10. Calculated isobaric melt composition, for the bulk compositions: (a) MM-3 at 15 kbar, this study; (b) MM-3 at 15 kbar calculated in pMELTS in NCFCMASOCrTi (details of the calculation are given in the Supplementary Data); (c) KR4003 at 30 kbar, this study. All plots show composition as a function of temperature (expressed as melt fraction *F*). Lines are calculated values, where each colour relates to a particular oxide content (wt %). For comparison, circles show the melt compositions for MM-3 from Falloon *et al.* (2008, and references therein) and for KR4003 from Walter (1998). The agreement with the experimental data for MM-3 is fairly good, that with KR4003 slightly less so. In all cases, calculated FeO is FeO only, whereas experimental FeO is FeO_{Total} (i.e. no allowance is made for Fe_2O_3 and no experimental Fe_2O_3 is reported).

It is commonly believed that mantle log fO_2 decreases with depth; a trend that matches the xenolith record (Fig. 14; e.g. Frost & McCammon, 2008, and references therein). Although this overall trend holds true in the melt model, in detail, log fO_2 is a product of the interplay of phase equilibria, pressure and temperature. It may be that these effects are smeared out within the xenolith record, where *P*, *T* and log fO_2 estimates are affected by uncertainty, disequilibria and complex thermal and metasomatic history. Figure 14 shows log fO_2 calculated along a lithospheric geothermal gradient in a garnet lherzolite for two bulk Fe_2O_3 values. Along the geotherm in the plotted pressure range, log fO_2 does decrease with increasing pressure. For the range of bulk Fe_2O_3 observed in mantle xenoliths (0·1–0·4 wt %) by Canil *et al.* (1994), the model log fO_2 matches the xenolith data well. It should be noted that the xenolith log fO_2 values reported by Frost & McCammon (2008), and references therein, have been incremented by a conservative +1 ΔQFM in Fig. 14 to reflect the revised garnet oxybarometer recalibration of Miller *et al.* (in review).

The effect of bulk mantle Fe_2O_3 on log fO_2 for a given pressure is shown in Fig. 15. As expected, decreasing Fe_2O_3 results in decreasing log fO_2. In this study, a mantle Fe_2O_3 of 0·3 wt % is assumed, based on the lithospheric mantle xenolith values of Canil *et al.* (1994); a value not well constrained for the convecting mantle. Figure 15 illustrates the high sensitivity of log fO_2 to small changes in bulk Fe_2O_3 when bulk Fe_2O_3 is lower than the mantle value used in this study (0·3 wt %). This sensitivity, combined with uncertainty in the bulk mantle composition, results in significant uncertainty in mantle log fO_2 for low-Fe_2O_3 peridotites.

Comparison with other models

Calculations in the current model are performed in THERMOCALC (Powell *et al.*, 1998), a program designed to calculate equilibrium phase equilibria but currently without the functionality to track fractional processes. A comparison between experimental data, this model and previously published models at selected pressures and melt fractions is presented in Table 4.

pMELTS, part of the MELTS family of thermodynamic models, is optimized for mantle melting-appropriate *P*–*T* conditions and bulk compositions (Ghiorso *et al.*, 2002). Used through the alphaMELTS front end (Smith & Asimow, 2005) it is very flexible, allowing trace elements to be tracked and the investigation of lithologies in more extensive component space (e.g. by the addition of TiO_2 and water). Unlike other models, it can provide information on phase relations at subsolidus conditions. It is conveniently set up to mimic mantle melting more realistically, following dynamic *P*–*T* paths and calculating fractional or equilibrium melting. The subsequent crystallization and fractionation of mantle melts can be examined in other MELTS models. However, for the specific task of melting mantle peridotite, it reproduces experimental compositions less well than our model and others, particularly at very low melt fractions and higher pressures (Table 4 and Fig. 8). The strengths and

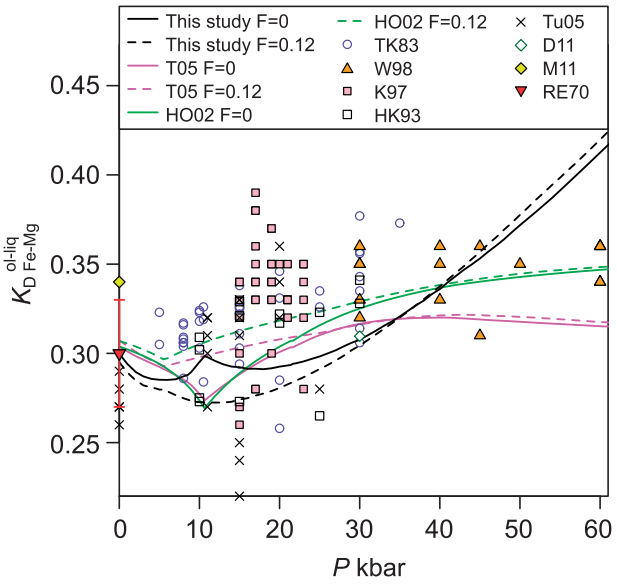

Fig. 11. Plot of $K_{D\,Fe\text{-}Mg}^{ol\text{-}liq}$ as a function of pressure. Continuous lines are calculated along the KLB-1 solidus (a nominal zero melt fraction); dashed lines are calculated along a 12% melt fraction isopleth. Black lines from this study. Points are experimental measured values. Experimental data point abbreviations: TK83, Takahashi & Kushiro (1983); W98, Walter (1998); K97, Kinzler (1997); HK93, Hirose & Kushiro (1993); Tu05, Tuff *et al.* (2005); D11, Davis *et al.* (2011); M11, Matzen *et al.* (2011); RE70, Roeder & Emslie (1970). All experiments are peridotite melting experiments, except Tu05, RE70 and M11, which are from basalt crystallization. The range of ±0·03 on the RE70 point is as suggested by Takahashi & Kushiro (1983). Lines for T05 and HO02 are calculated from the liquid compositions of this study at $F=0$ (solidus) and 0·12 melt fraction from the expressions of T05, Toplis (2005) and HO02, Herzberg & O'Hara (2002). The downward inflection seen in T05 and HO02 $F=0$ at 10 kbar reflects the unusual low fraction liquid composition close to the plagioclase-out boundary. A good agreement in $K_{D\,Fe\text{-}Mg}^{ol\text{-}liq}$ is seen between this study and experimental points and previous formulations up to 40 kbar.

weaknesses of pMELTS and related models have been discussed in detail elsewhere (Ghiorso *et al.*, 2002).

Another approach uses empirical descriptions of liquidus phase relations to predict when phases become stable in a crystallizing assemblage [e.g. PETROLOG (Danyushevsky & Plechov, 2011), COMAGMAT (Ariskin *et al.*, 1993) and the SPICEs family (MAGPOX, MAGFOX, FXMOTR; Longhi, 1991; Davenport *et al.*, 2014)]. MAGPOX, which is tested here, calculates equilibrium crystallization for compositions where olivine is the liquidus phase at a given pressure. It is often used in meteoritics and planetary studies; for example, in understanding magma ocean crystallization. Table 4 indicates a reasonable match to an experimental melt of KLB-1 at $F=0{\cdot}2$ and $P=10$ kbar. However, this family of models is appropriate to high melt fractions and may reach unrealistic compositions at lower melt fraction, and thus is less useful for mantle melting and more useful for crystallizing liquids.

An alternative approach to model mantle melt composition uses an empirical formulation of temperature and major element chemistry (e.g. McKenzie & Bickle, 1988; Kinzler & Grove, 1992; Herzberg & O'Hara, 2002). Herzberg & O'Hara (2002) proposed a forward model of primary melt compositions represented in CMAS based on a parameterization of a large experimental database, which provides a means by which olivine fractionation can be accounted for in basalt compositions, and so allows the temperature and composition of primary melts to be deduced from natural melt compositions (e.g. Herzberg *et al.*, 2007). Kinzler & Grove (1992) provided equations for the temperature and eight-component major element chemistry of a melt in equilibrium with plagioclase or spinel lherzolite, for a given pressure and four melt compositional variables. Updated parameterizations were given by Till *et al.* (2012) for plagioclase and spinel lherzolites and by Grove *et al.* (2013) for garnet lherzolites. This approach allows for variation in bulk composition, although it requires pre-existing knowledge of some melt compositional variables. Predicted melt compositions show an excellent agreement with experimental melts at low melt fraction (Table 4 and Fig. 8) when known compositional variables are supplied, so the melt composition is not fully independently predicted. These models are appropriate for only the four-phase assemblage [cpx, opx, ol, Al-phase], and therefore cease to work once a phase is exhausted from the residue.

The tested models perform adequately in predicting mantle melts, each with their own strengths and weaknesses. The model presented here with calculations performed in THERMOCALC is no exception. It has been developed for mantle peridotite subsolidus and melting phase relations. It performs well at this task compared with other models, and works over a full melt fraction range, although the reappearance of tiny amounts of spinel at high melt fractions may reflect a model deficiency. In particular, it is more effective than other models at predicting the composition of very low melt fraction melts, which is important for understanding fractional mantle melting processes. The model also performs well from 0·001 to 60 kbar, whereas pMELTS has a more restricted recommended range of 10–30 kbar (Ghiorso *et al.*, 2002). However, the model is restricted to a relatively narrow range in liquid composition (basaltic to ultramafic), and as yet there is no provision in THERMOCALC for polybaric fractional melting.

CONCLUSIONS AND SUMMARY

A simple thermodynamic model (TiO_2, K_2O, H_2O or CO_2 were not considered) has been developed for peridotite bulk compositions, including melting behaviour, for the system NCFMASOCr in the range 0–60 kbar from 800°C to liquidus temperatures. It was calibrated on a rather small number of experimental constraints, allowing it to be tested over a wide set of experimental and natural observations.

Findings of this study

The new model allows exploration of the phase equilibria and melting behaviour of mantle peridotite (and in

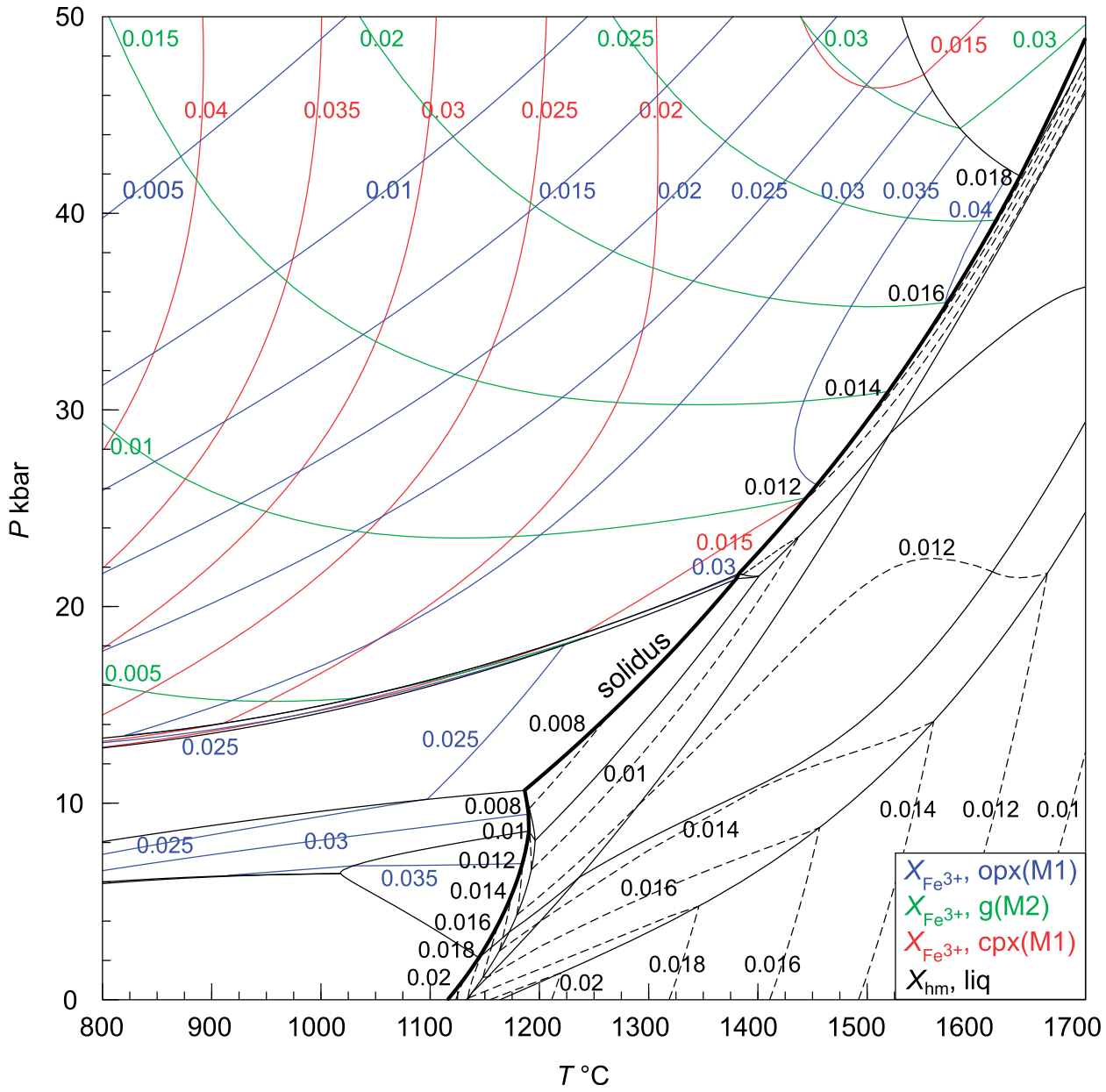

Fig. 12. Isopleths of constant phase ferric iron content in *P–T* space. Blue lines, Fe in the opx M1 site; green lines, Fe in garnet M2 sites; red lines, Fe in cpx M1 sites. Dashed black lines show the molar proportion of the hm ($FeO_{1·5}$) end-member in the liquid, which approximately relates to wt % Fe_2O_3 in the melt by the relationship: wt % $Fe_2O_3 \approx 46·6 \times X_{hm}$. Phase boundaries are indicated by black lines and correspond to those in Fig. 1. Isopleths are not shown in fields where the phase is absent, or for solid phases above the solidus. It should be noted that beneath the g-out boundary, isopleths for Fe in cpx(M1) are not present because this variable remains near-constant in garnet-absent assemblages. Isopleths for $FeO_{1·5}$ in melt show a small range with variability largely confined to low pressures just above the solidus.

particular the KLB-1 composition), and provides interesting observations that may not easily be accessible through experimental petrology or from natural samples. A miscibility gap between Al-rich and Cr-rich spinels has been identified at low temperature, in agreement with the observation that Cr-rich spinel is often found as the liquidus phase in primitive melts (low pressure), whereas Al-rich spinel is the stable phase found in spinel-bearing mantle xenoliths (higher pressure). The model predicts that no mineral compositions are particularly pressure-sensitive in garnet-free spinel lherzolites (where there is no garnet or plagioclase to provide a density contrast with other silicates), illustrating the difficulty in finding a suitable barometer for spinel lherzolite xenoliths. The model also indicates that the spinel–garnet transition may be rather narrow in the mantle, and at lower pressures than suggested by previous studies; increasing bulk Cr and Fe^{3+} broadens the transition and shifts it to higher pressures. A cusp in solidus temperature is identified at the plagioclase–spinel transition, caused by the increasing albite component of high-pressure plagioclase. Finally, the complex way in

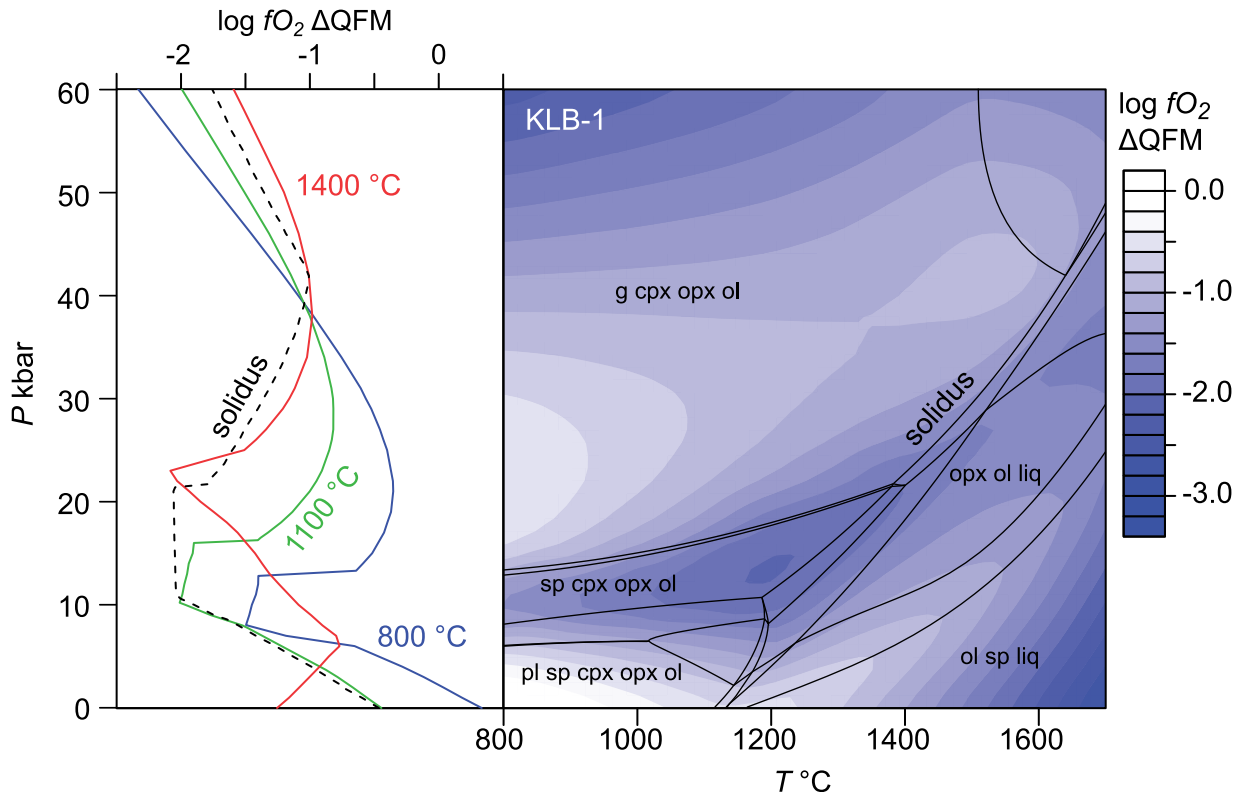

Fig. 13. Plot of log fO_2 relative to QFM as a function of pressure for three isothermal sections and along the solidus (left-hand panel), and log fO_2 relative to QFM as a function of pressure and temperature (right-hand panel). Lines in the left-hand plot are isothermal sections through the right-hand plot, whose inflections correspond to phase boundaries. It is clear that mantle log fO_2 does not simply vary with pressure and temperature; rather, it is a complex function of pressure, temperature and phase assemblage. A peculiarity is the initial increase in log fO_2 with increasing pressure in the [g cpx opx ol] field, before the expected decrease with further increasing pressure. Also of note is the rather extreme log fO_2 contrast between different low-pressure phase assemblages. Along the solidus, log fO_2 can either increase or decrease with pressure, depending on assemblage, although it is anticipated that at pressures higher than the limits of this plot, log fO_2 will continue to decrease with pressure.

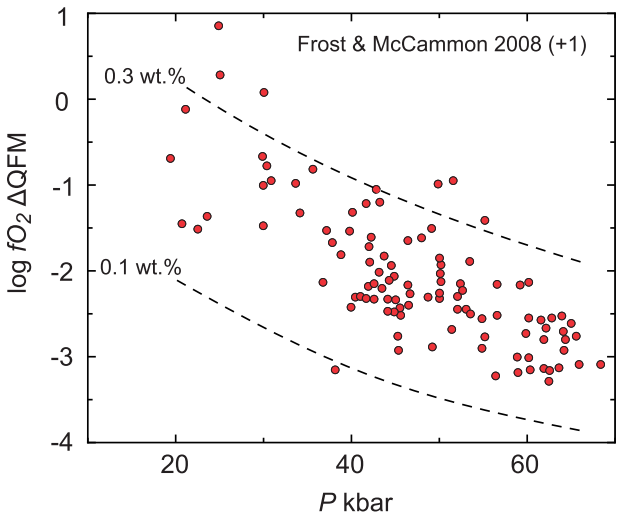

Fig. 14. Plot of log fO_2 relative to QFM as a function of pressure from Frost & McCammon (2008) for mantle xenoliths. All values have been modified by + 1 log unit to account for the recalibration of log fO_2 from Miller *et al.* (in review). Dashed lines are calculations along a *P–T* gradient from 30 kbar and 800°C to 60 kbar and 1300°C, for KLB-1 peridotite with two Fe_2O_3 compositions. Calculations thus suggest that the spread of natural xenolith data indicates bulk oxygen contents between 0·1 and 0·4 wt % Fe_2O_3, exactly as found by Canil *et al.* (1994).

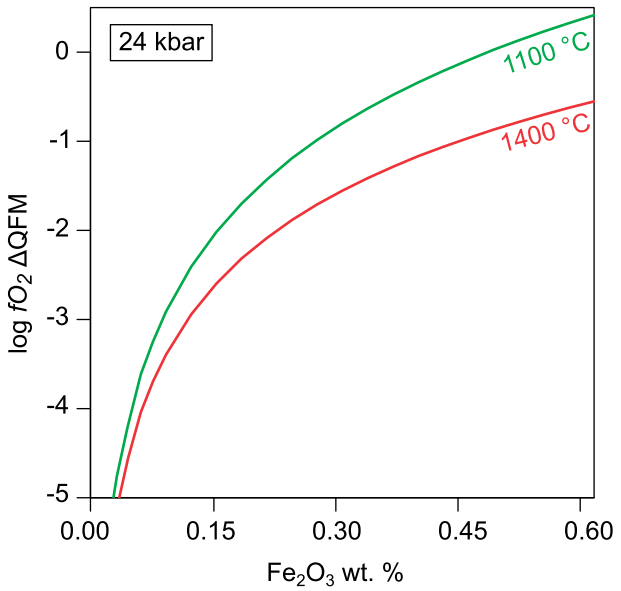

Fig. 15. Plot of log fO_2 relative to QFM as a function of bulk Fe_2O_3, at constant pressure and temperature, calculated for KLB-1. The two lines show calculations performed at 1100°C and 1400°C, both for a garnet lherzolite assemblage. This shows the particular sensitivity of mantle log fO_2 to bulk Fe_2O_3 lower than around 0·30 wt % (i.e. the KLB-1 composition).

Table 4: Partial melt compositions of KLB-1 at a range of pressures P and melt fractions F calculated by various models

	KLB-1, $P=10$ kbar, $F=0$				KLB-1, $P=10$ kbar, $F=0{\cdot}2$			
Type:	Experiment	Model			Experiment	Model		
Ref.:	F08*	This study	pMELTS	T12‡	HK93 run16	This study	pMELTS	MAGPOX
T(°C):	1268	1188	1230	1252	1350	1311	1377	1398
SiO_2	51·45	51·19	54·07	51·80	50·67	49·11	49·47	50·87
TiO_2	1·45	n.a.	0·49	0·84	0·42	n.a.	0·48	0·32
Al_2O_3	19·05	19·23	19·58	18·82	14·61	12·83	13·88	11·71
Cr_2O_3	0·09	0·09	0·18	n.a.	0·28	0·40	0·13	0·03
Fe_2O_3	n.a.	0·36	0·26	n.a.	n.a.	0·56	1·05	0·74
FeO†	n.a.	5·71	3·49	n.a.	n.a.	8·71	7·12	8·05
FeO^T	5·42	6·03	3·72	5·63	7·64	9·21	8·06	8·72
MgO	8·28	8·50	7·19	8·39	13·39	13·84	14·50	15·86
CaO	9·39	9·62	4·23	9·35	11·17	13·09	11·89	11·16
Na_2O	4·35	5·31	10·52	5·16	1·50	1·45	1·48	1·26

	KLB-1, $P=30$ kbar, $F=0$				KLB-1, $P=30$ kbar, $F=0{\cdot}17$		
Type:	Experiment	Model			Experiment	Model	
Ref.:	D11	This study	pMELTS	G13‡	HK93 run25	This study	pMELTS
T(°C):	1445	1508	1496	1527	1500	1531	1855
SiO_2	44·77	46·98	40·99	45·71	45·67	46·97	40·46
TiO_2	2·45	n.a.	1·17	0·84	0·99	n.a.	0·48
Al_2O_3	12·70	12·88	7·93	12·72	14·33	11·35	6·85
Cr_2O_3	0·12	0·14	0·44	n.a.	0·21	0·38	0·15
Fe_2O_3	n.a.	0·64	1·14	n.a.	n.a.	0·49	1·08
FeO	n.a.	10·06	13·31	n.a.	n.a.	9·77	13·56
FeO_T	9·72	10·64	14·34	11·41	9·59	10·21	14·53
MgO	15·78	15·35	21·47	17·41	16·73	17·03	26·97
CaO	10·80	11·56	4·77	9·86	10·64	12·43	8·82
Na_2O	2·52	2·39	8·78	2·04	1·80	1·58	1·62

HK93, Hirose & Kushiro (1993); F08, Falloon *et al.* (2008); D11, Davis *et al.* (2011); T12, Till *et al.* (2012); G13, Grove *et al.* (2013). n.a., not applicable.

*FO8 experiments on MM-3, a bulk composition similar to KLB-1.

†Total Fe expressed as FeO; where a model predicts FeO and Fe_2O_3 separately, FeO_T is shown in addition to FeO_T.

‡As in Fig. 8, T12 and G13 are calculated using Mg# and NaK# of the relevant melts from this study, so their melt compositions are not completely independently predicted.

which mantle log fO_2 varies with mineral assemblage, P, T and bulk Fe_2O_3 has been identified.

Model uses and bounds

It is concluded that this, albeit rudimentary, model provides an effective means of examining mantle phase equilibria and melting. It should primarily be used to interpolate between P–T–X conditions of experimental studies of upper mantle peridotite. This allows the exploration of parameter space that is impractical to investigate experimentally; for example, subsolidus or low-temperature conditions that are difficult to equilibrate and are important for understanding the xenolith record, and very low melt fractions that are important for understanding fractional melting. The model can be used to investigate magma ocean crystallization and planetary evolution, and to understand the intricacies of mantle and melt fO_2.

The model can be used to explore the origin of basalts. For example, the effect of varying mantle potential temperature T_p on major element melt composition can be assessed, and parameters that inform trace element models can be derived. This study has focused on equilibrium melting behaviour, but fractional melting of the mantle could be explored by accounting for the depletion of the bulk composition.

This model should be used only in the pressure range of 0·001–60 kbar, which reflects the range of experimental data used in the calibration. Some aspects, such as the solidus position and mineral modes, are valid to higher pressures, and others, such as solid–liquid Mg–Fe partitioning, work less well at high pressures. The model is calibrated for peridotite, specifically KLB-1, although it should work well for other peridotite compositions, including more depleted ones. The entropy formalism adopted for the liquid is probably limited to compositions close to basalt and its use is not advised for inve-stigating melting of more silica-rich bulk compositions, such as eclogite, where it may produce unreliable results.

The model is presented in the simple NCFMASOCr system. This begins to approximate a real, complex system, unlike the MAS, CMAS and CFMAS predecessors. However, the effects of Ti and K are not examined, and will have a minor effect on phase equilibria and liquid composition (Davis & Hirschmann, 2013). Volatiles such as H_2O and CO_2 have been shown to have important effects on phase equilibria, melt compositions, and the

pressure and temperature of melting onset (e.g. Green, 1973; Eggler, 1976; Gaetani & Grove, 1998; Dasgupta & Hirschmann, 2010). There is scope for future developments to the model to incorporate more components, more end-members and more complex mixing models as experimental studies continue to refine and inform an understanding of mantle phase equilibria.

After the review stages of this paper the publication of Ueki & Iwamori (2014) became available. This offers an alternative model for exploring phase relationships limited to spinel lherzolite melting in the smaller FCMASO subsystem, but has not been evaluated in our work.

ACKNOWLEDGEMENTS

Oliver Shorttle, Sally Gibson, and David Neave are thanked for helpful discussions on aspects of mantle petrology and geochemistry; John Maclennan is thanked for constructive suggestions on an earlier draft of this paper. Claude Herzberg and Paul Asimow are thanked for perceptive and helpful reviews, which led to significant improvements to the presentation.

FUNDING

This work was supported by a Natural Environment Research Council studentship [NE/J500070/1] to E.S.J. and Natural Environment Research Council grant [NE/J021539/1] to T.J.B.H.

SUPPLEMENTARY DATA

Supplementary data for this paper are available at *Journal of Petrology* online.

REFERENCES

Ariskin, A. A., Frenkel, M. Y., Barmina, G. S. & Nielsen, R. L. (1993). COMAGMAT—A FORTRAN program to model magma differentiation processes. *Computers and Geosciences* **19**, 1155–1170.

Asimow, P. D. & Ghiorso, M. S. (1998). Algorithmic modifications extending MELTS to calculate subsolidus phase relations. *American Mineralogist* **83**, 1127–1131.

Blundy, J. D., Falloon, T. J., Wood, B. J. & Dalton, J. A. (1995). Sodium partitioning between clinopyroxene and silicate melts. *Journal of Geophysical Research* **100**, 15501–15515.

Borghini, G., Fumagalli, P. & Rampone, E. (2010). The stability of plagioclase in the upper mantle: subsolidus experiments on fertile and depleted lherzolite. *Journal of Petrology* **51**, 229–254.

Bryndzia, L. T. & Wood, B. J. (1990). Oxygen thermobarometry of abyssal spinel peridotites: the redox state and C–O–H volatile composition of the Earth's sub-oceanic upper mantle. *American Journal of Science* **290**, 1093–1116.

Canil, D. (1992). Orthopyroxene stability along the peridotite solidus and the origin of cratonic lithosphere beneath southern Africa. *Earth and Planetary Science Letters* **111**, 83–95.

Canil, D. & O'Neill, H. St. C. (1996). Distribution of ferric iron in some upper-mantle assemblages. *Journal of Petrology* **37**, 609–635.

Canil, D., O'Neill, H. St. C. Pearson, D. G., Rudnick, R. L., McDonough, W. F. & Carswell, D. A. (1994). Ferric iron in peridotites and mantle oxidation states. *Earth and Planetary Science Letters* **123**, 205–220.

Cottrell, E. & Kelley, K. A. (2011). The oxidation state of Fe in MORB glasses and the oxygen fugacity of the upper mantle. *Earth and Planetary Science Letters* **305**, 270–282.

Dachs, E., Geiger, C. A. & Benisek, A. (2012). Almandine: Lattice and non-lattice heat capacity behavior and standard thermodynamic properties. *American Mineralogist* **97**, 1771–1782.

Danyushevsky, L. V. & Plechov, P. (2011). Petrolog3: integrated software for modeling crystallization processes. *Geochemistry, Geophysics, Geosystems* **12**, Q07021.

Dasgupta, R. & Hirschmann, M. M. (2010). The deep carbon cycle and melting in Earth's interior. *Earth and Planetary Science Letters* **298**, 1–13.

Davenport, J., Longhi, J., Neal, C. R., Joliff, B. & Bolster, D. (2014). Simulating planetary igneous crystallization environments (SPICEs): A suite of igneous crystallization programs. Proceedings of 45th Lunar and Planetary Science Conference, p. 1111.

Davis, F. A. & Hirschmann, M. M. (2013). The effects of K_2O on the compositions of near-solidus melts of garnet peridotite at 3 GPa and the origin of basalts from enriched mantle. *Contributions to Mineralogy and Petrology* **166**, 1029–1046.

Davis, F. A., Tangeman, J. A., Tenner, T. J. & Hirschmann, M. M. (2009). The composition of KLB-1 peridotite. *American Mineralogist* **94**, 176–180.

Davis, F. A., Hirschmann, M. M. & Humayun, M. (2011). The composition of the incipient partial melt of garnet peridotite at 3 GPa and the origin of OIB. *Earth and Planetary Science Letters* **308**, 380–390.

Eggler, D. H. (1976). Does CO_2 cause partial melting in the low-velocity layer of the mantle?. *Geology* **4**, 69–72.

Falloon, T. J., Green, D. H., Danyushevsky, L. V. & McNeill, A. W. (2008). The composition of near-solidus partial melts of fertile peridotite at 1 and 1·5 GPa: implications for the petrogenesis of MORB. *Journal of Petrology* **49**, 591–613.

Foulger, G. R. & Anderson, D. L. (2005). A cool model for the Iceland hotspot. *Journal of Volcanology and Geothermal Research* **141**, 1–22.

Frost, D. J. & McCammon, C. A. (2008). The redox state of Earth's mantle. *Annual Review of Earth and Planetary Sciences* **36**, 389–420.

Gaetani, G. A. & Grove, T. L. (1998). The influence of water on melting of mantle peridotite. *Contributions to Mineralogy and Petrology* **131**, 323–346.

Ganguly, J., Cheng, W. & Tirone, M. (1996). Thermodynamics of aluminosilicate garnet solid solution: new experimental data, an optimized model, and thermometric applications. *Contributions to Mineralogy and Petrology* **126**, 137–151.

Gaskell, D. R. (2012). *Introduction to the Thermodynamics of Materials*, 5th edn. London: Taylor & Francis.

Gasparik, T. (1984). Two-pyroxene thermobarometry with new experimental data in the system $CaO–MgO–Al_2O_3–SiO_2$. *Contributions to Mineralogy and Petrology* **87**, 87–97.

Gasparik, T. & Newton, R. C. (1984). The reversed alumina contents of orthopyroxene in equilibrium with spinel and forsterite in the system $MgO–Al_2O_3–SiO_2$. *Contributions to Mineralogy and Petrology* **85**, 186–196.

Geiger, C. A., Newton, R. C. & Kleppa, O. J. (1987). Enthalpy of mixing of synthetic almandine–grossular and almandine–pyrope garnets from high-temperature solution calorimetry. *Geochimica et Cosmochimica Acta* **51**, 1755–1763.

Ghiorso, M. S. & Sack, R. O. (1995). Chemical mass transfer in magmatic processes. IV. A revised and internally consistent thermodynamic model for the interpolation and extrapolation of liquid–solid equilibria in magmatic systems at

elevated temperatures and pressures. *Contributions to Mineralogy and Petrology* **119**, 197–212.

Ghiorso, M. S., Hirschmann, M. M., Reiners, P. W. & Kress, V. C., III (2002). The pMELTS: A revision of MELTS for improved calculation of phase relations and major element partitioning related to partial melting of the mantle to 3 GPa. *Geochemistry, Geophysics, Geosystems* **3**, doi:10.1029/2001GC000217.

Green, D. H. (1973). Experimental melting studies on a model upper mantle composition at high pressure under water-saturated and water-undersaturated conditions. *Earth and Planetary Science Letters* **19**, 37–53.

Green, E. C. R., Holland, T. J. B., Powell, R. & White, R. W. (2012a). Garnet and spinel lherzolite assemblages in $MgO–Al_2O_3–SiO_2$ and $CaO–MgO–Al_2O_3–SiO_2$: thermodynamic models and an experimental conflict. *Journal of Metamorphic Geology* **30**, 561–577.

Green, E. C. R., Holland, T. J. B. & Powell, R. (2012b). A thermodynamic model for silicate melt in $CaO–MgO–Al_2O_3–SiO_2$ to 50 kbar and 1800°C. *Journal of Metamorphic Geology* **30**, 579–597.

Grove, T. L., Holbig, E. S., Barr, J. A., Till, C. B. & Krawczynski, M. J. (2013). Melts of garnet lherzolite: experiments, models and comparison to melts of pyroxenite and carbonated lherzolite. *Contributions to Mineralogy and Petrology* **166**, 887–910.

Gudmundsson, G. & Wood, B. J. (1995). Experimental Tests of Garnet Peridotite Oxygen Barometry. *Contributions to Mineralogy and Petrology* **119**, 56–67.

Hackler, R. T. & Wood, B. J. (1989). Experimental determination of Fe and Mg exchange between garnet and olivine and estimation of Fe–Mg mixing properties in garnet. *American Mineralogist* **74**, 994–999.

Herzberg, C. & O'Hara, M. J. (2002). Plume-associated ultramafic magmas of Phanerozoic age. *Journal of Petrology* **43**, 1857–1883.

Herzberg, C., Gasparik, T. & Sawamoto, H. (1990). Origin of mantle peridotite: Constraints from melting experiments to 16·5 GPa. *Journal of Geophysical Research* **95**, 15779–15803.

Herzberg, C., Raterron, P. & Zhang, J. (2000). New experimental observations on the anhydrous solidus for peridotite KLB-1. *Geochemistry, Geophysics, Geosystems* **1**, 2000GC000089.

Herzberg, C., Asimow, P. D., Arndt, N., Niu, Y., Lesher, C. M., Fitton, J. G., Cheadle, M. J. & Saunders, A. D. (2007). Temperatures in ambient mantle and plumes: Constraints from basalts, picrites, and komatiites. *Geochemistry, Geophysics, Geosystems* **8**, Q02006.

Herzberg, C. & Zhang, J. (1996). Melting experiments on anhydrous peridotite KLB-1: Compositions of magmas in the upper mantle and transition zone. *Journal of Geophysical Research* **101**, 8271–8295.

Hirose, K. & Kushiro, I. (1993). Partial melting of dry peridotites at high pressures: Determination of compositions of melts segregated from peridotite using aggregates of diamond. *Earth and Planetary Science Letters* **114**, 477–489.

Hirschmann, M. M. (2000). Mantle solidus: Experimental constraints and the effects of peridotite composition. *Geochemistry, Geophysics, Geosystems* **1**, 2000GC000070.

Holland, T. J. B. & Powell, R. (2001). Calculation of phase relations involving haplogranitic melts using an internally consistent thermodynamic dataset. *Journal of Petrology* **42**, 673–683.

Holland, T. J. B. & Powell, R. (2003). Activity–composition relations for phases in petrological calculations: an asymmetric multicomponent formulation. *Contributions to Mineralogy and Petrology* **145**, 492–501.

Holland, T. J. B. & Powell, R. (2011). An improved and extended internally-consistent thermodynamic dataset for phases of petrological interest, involving a new equation of state for solids. *Journal of Metamorphic Geology* **29**, 333–383.

Holland, T. J. B., Hudson, N. F. C., Powell, R. & Harte, B. (2013). New thermodynamic models and calculated phase equilibria in NCFMAS for basic and ultrabasic compositions through the transition zone into the uppermost lower mantle. *Journal of Petrology* **54**, 1901–1920.

Ionov, D. A. (2004). Chemical variations in peridotite xenoliths from Vitim, Siberia: inferences for REE and Hf behaviour in the garnet facies upper mantle. *Journal of Petrology* **45**, 343–367.

Jayasuriya, K. D., O'Neill, H. St. C. Berry, A. J. & Campbell, S. J. (2004). A Mossbauer study of the oxidation state of Fe in silicate melts. *American Mineralogist* **89**, 1597–1609.

Jenkins, D. M. & Newton, R. C. (1979). Experimental determination of the spinel peridotite to garnet peridotite inversion at 900°C and 1000°C in the system $CaO–MgO–Al_2O_3–SiO_2$, and at 900°C with natural garnet and olivine. *Contributions to Mineralogy and Petrology* **68**, 407–419.

Kantor, A., Kantor, I., Merlini, M., Glazyrin, K., Prescher, C., Hanfland, M. & Dubrovinsky, L. (2012). High-pressure structural studies of eskolaite by means of single-crystal X-ray diffraction. *American Mineralogist* **97**, 1764–1770.

Katz, R. F., Spiegelman, M. & Langmuir, C. H. (2003). A new parameterization of hydrous mantle melting. *Geochemistry, Geophysics, Geosystems* **4**, doi:10.1029/2002GC000433.

Kinzler, R. J. (1997). Melting of mantle peridotite at pressures approaching the spinel to garnet transition: Application to mid-ocean ridge basalt petrogenesis. *Journal of Geophysical Research* **102**, 853–874.

Kinzler, R. J. & Grove, T. L. (1992). Primary magmas of mid-ocean ridge basalts 1. Experiments and methods. *Journal of Geophysical Research* **97**, 6885–6906.

Klemme, S. (2004). The influence of Cr on the garnet–spinel transition in the Earth's mantle: experiments in the system $MgO–Cr_2O_3–SiO_2$ and thermodynamic modelling. *Lithos* **77**, 639–646.

Klemme, S. & O'Neill, H. St. C. (2000). The near-solidus transition from garnet lherzolite to spinel lherzolite. *Contributions to Mineralogy and Petrology* **138**, 237–248.

Klemme, S., Ivanic, T. J., Connolly, J. A. D. & Harte, B. (2009). Thermodynamic modelling of Cr-bearing garnets with implications for diamond inclusions and peridotite xenoliths. *Lithos* **112**, Supplement 2, 986–991.

Koziol, A. M. (1990). Activity–composition relationships of binary Ca–Fe and Ca–Mn garnets determined by reversed, displaced equilibrium experiments. *American Mineralogist* **75**, 319–327.

Koziol, A. M. & Bohlen, S. R. (1992). Solution properties of almandine–pyrope garnet as determined by phase equilibrium experiments. *American Mineralogist* **77**, 765–773.

Kress, V. C. & Carmichael, I. S. E. (1991). The compressibility of silicate liquids containing Fe_2O_3 and the effect of composition, temperature, oxygen fugacity and pressure on their redox states. *Contributions to Mineralogy and Petrology* **108**, 82–92.

Longhi, J. (1991). Comparative liquidus equilibria of hypersthene-normative basalts at low pressure. *American Mineralogist* **76**, 785–800.

Longhi, J. (2002). Some phase equilibrium systematics of lherzolite melting: I. *Geochemistry, Geophysics, Geosystems* **3**, doi:10.1029/2001GC000204.

Mattioli, G. S. & Bishop, F. C. (1984). Experimental determination of the chromium–aluminum mixing parameter in garnet. *Geochimica et Cosmochimica Acta* **48**, 1367–1371.

Matzen, A. K., Baker, M. B., Beckett, J. R. & Stolper, E. M. (2011). Fe–Mg partitioning between olivine and high-magnesian

melts and the nature of Hawaiian parental liquids. *Journal of Petrology* **52**, 1243–1263.
McKenzie, D. & Bickle, M. J. (1988). The volume and composition of melt generated by extension of the lithosphere. *Journal of Petrology* **29**, 625–679.
Mibe, K., Fujii, T., Yasuda, A. & Ono, S. (2006). Mg–Fe partitioning between olivine and ultramafic melts at high pressures. *Geochimica et Cosmochimica Acta* **70**, 757–766.
Miller, W., Holland, T. J. B. & Gibson, S. A. (2015). Multiple-reaction oxygen barometry for mantle peridotite: an internally-consistent thermodynamic model for reactions and garnet solid-solutions, with applications to the oxidation state of lithospheric mantle. *Contributions to Mineralogy & Petrology*, in review.
Newton, R. C., Charlu, T. V. & Kleppa, O. J. (1977). Thermochemistry of high pressure garnets and clinopyroxenes in the system CaO–MgO–Al_2O_3–SiO_2. *Geochimica et Cosmochimica Acta* **41**, 369–377.
Newton, R. C., Charlu, T. V. & Kleppa, O. J. (1980). Thermochemistry of the high structural state plagioclases. *Geochimica et Cosmochimica Acta* **44**, 933–941.
Nimis, P., Goncharov, A., Ionov, D. A. & McCammon, C. (2015). Fe^{3+} partitioning systematics between orthopyroxene and garnet in mantle peridotite xenoliths and implications for thermobarometry of oxidized and reduced mantle rocks. *Contributions to Mineralogy and Petrology* **169**, 6.
O'Neill, H. St. C. Berry, A. J., McCammon, C. C., Jayasuriya, K. D., Campbell, S. J. & Foran, G. (2006). An experimental determination of the effect of pressure on the $Fe^{3+}/\Sigma Fe$ ratio of an anhydrous silicate melt to 3·0 GPa. *American Mineralogist* **91**, 404–412.
Perkins, D. P. & Newton, R. C. (1980). The compositions of coexisting pyroxenes and garnet in the system CaO–MgO–Al_2O_3–SiO_2 at 900–1100°C and high pressures. *Contributions to Mineralogy and Petrology* **75**, 291–300.
Powell, R., Holland, T. & Worley, B. (1998). Calculating phase diagrams involving solid solutions via non-linear equations, with examples using THERMOCALC. *Journal of Metamorphic Geology* **16**, 577–588.
Powell, R., White, R. W., Green, E. C. R., Holland, T. J. B. & Diener, J. F. A. (2014). On parameterizing thermodynamic descriptions of minerals for petrological calculations. *Journal of Metamorphic Geology* **32**, 245–260.
Pownceby, M. I., Wall, V. J. & O'Neill, H. St. C. (1987). Fe–Mn partitioning between garnet and ilmenite: experimental calibration and applications. *Contributions to Mineralogy and Petrology* **97**,116–126.
Robie, R. A., Hemingway, B. S. & Fisher, J. R. (1978). Thermodynamic properties of minerals and related substances at 298·15 K and 1 bar (10^5 Pascals) pressure and at higher temperatures. *US Geological Survey Bulletin* **1452**, 456 pp.
Robinson, J. A. C. & Wood, B. J. (1998). The depth of the spinel to garnet transition at the peridotite solidus. *Earth and Planetary Science Letters* **164**, 277–284.
Robinson, J. A. C., Wood, B. J. & Blundy, J. D. (1998). The Beginning of Melting of Fertile and Depleted Peridotite at 1.5 GPa. *Earth and Planetary Science Letters* **155**, 97–111.
Roeder, P. L. & Emslie, R. F. (1970). Olivine–liquid equilibrium. *Contributions to Mineralogy and Petrology* **29**, 275–289.
Smith, P. M. & Asimow, P. D. (2005). Adiabat_1ph: A new public front-end to the MELTS, pMELTS, and pHMELTS models. *Geochemistry, Geophysics, Geosystems* **6**, Q02004.
Takahashi, E. & Kushiro, I. (1983). Melting of a dry peridotite at high pressures and basalt magma genesis. *American Mineralogist* **68**, 859–879.
Takahashi, E. (1986). Melting of a Dry Peridotite KLB-1 up to 14 GPa: Implications on the Origin of Peridotitic Upper Mantle. *Journal of Geophysical Research: Solid Earth* **91**, 9367–9382.
Takahashi, E., Shimazaki, T., Tsuzaki, Y. & Yoshida, H. (1993). Melting study of a peridotite KLB-1 to 6·5 GPa, and the origin of basaltic magmas. *Philosophical Transactions of the Royal Society of London, Series A* **342**, 105–120.
Taura, H., Yurimoto, H., Kurita, K. & Sueno, S. (1998). Pressure dependence on partition coefficients for trace elements between olivine and the coexisting melts. *Physics and Chemistry of Minerals* **25**, 469–484.
Till, C. B., Grove, T. L. & Krawczynski, M. J. (2012). A melting model for variably depleted and enriched lherzolite in the plagioclase and spinel stability fields. *Journal of Geophysical Research* **117**, B06206.
Toplis, M. J. (2005). The thermodynamics of iron and magnesium partitioning between olivine and liquid: criteria for assessing and predicting equilibrium in natural and experimental systems. *Contributions to Mineralogy and Petrology* **149**, 22–39.
Tuff, J., Takahashi, E. & Gibson, S. A. (2005). Experimental constraints on the role of garnet pyroxenite in the genesis of high-Fe mantle plume derived melts. *Journal of Petrology* **46**, 2023–2058.
Ueki, K. & Iwamori, H. (2014). Thermodynamic calculations of the polybaric melting phase relations of spinel lherzolite. *Geochemistry, Geophysics, Geosystems* **15**, 5015–5033.
Walter, M. J. (1998). Melting of garnet peridotite and the origin of komatiite and depleted lithosphere. *Journal of Petrology* **39**, 29–60.
Wijbrans, C. J., Niehaus, O., Rohrbach, A., Pöttgen, R. & Klemme, S. (2014). Thermodynamic and magnetic properties of knorringite garnet ($Mg_3Cr_2Si_3O_{12}$) based on low-temperature calorimetry and magnetic susceptibility measurements. *Physics and Chemistry of Minerals* **41**, 341–346.
Wood, B. J. (1988). Activity measurements and excess entropy–volume relationships for pyrope–grossular garnets. *Journal of Geology* **96**, 721–729.
Wood, B. J. & Kleppa, O. J. (1984). Chromium–aluminum mixing in garnet: A thermochemical study. *Geochimica et Cosmochimica Acta* **48**, 1373–1375.
Woodland, A. B. (2009). Ferric iron contents of clinopyroxene from cratonic mantle and partitioning behaviour with garnet. *Lithos* **112S**, 1143–1149.
Woodland, A. B. & Koch, M. (2003). Variation in oxygen fugacity with depth in the upper mantle beneath the Kaapvaal craton, Southern Africa. *Earth and Planetary Science Letters* **214**, 295–310.
Woodland, A. B. & O'Neill, H. St. C. (1993). Synthesis and stability of $Fe^{2+}{}_3Fe^{3+}{}_2Si_3O_{12}$ garnet and phase relations with $Fe_3Al_2Si_3O_{12}$–$Fe^{2+}{}_3Fe^{3+}{}_2Si_3O_{12}$ solutions. *American Mineralogist* **78**, 1002–1015.
Woodland, A. B. & Peltonen, P. (1999). Ferric iron contents of garnet and clinopyroxene and estimated oxygen fugacities of peridotite xenoliths from the Eastern Finland Kimberlite Province. In: Gurney, J. J., Gurney, J. M., Pasco, M. D. & Richardson, S. H. (eds), P. H. Nixon Volume, Proceedings of the 7th Kimberlite Conference. Cape Town: Redroof, pp. 904–911.
Zhang, J. & Herzberg, C. T. (1994). Melting experiments on anhydrous peridotite KLB-1 from 5·0 to 22·5 GPa. *Journal of Geophysical Research* **99**, 17729–17742.

APPENDIX

The thermodynamic mixing properties of solid and melt solutions are provided here. The updated

Table A1: Interaction energies for melt end-members (kJ)

W	*a*	*b*	*c*
q, di	26 (3)	0	–0·4 (0·1)
q, jd	–10 (3)	0	0
q, ct	–10 (3)	0	0
q, fo	–25 (4)	0	–0·1 (0·1)
q, fa	–7 (4)	0	0
di, ct	–2 (3)	0	0
di, fo	24 (4)	0	0·2 (0·1)
di, fa	17 (4)	0	0
ct, fo	–1 (2)	0	0·1 (0·1)
fo, fa	9 (2)	0	0

Table A2: Increments (in kJ) to Gibbs energies of end-members in the dataset of Holland & Powell (2011)

Δ_i	*a*	*b*	*c*	Ref.
q	4·0 (0·9)	0	–0·43 (0·05)	2 qL
di	–6·7 (0·8)	0	0·17 (0·04)	diL
jd	18·7 (1·1)	0	–0·16 (0·04)	abL – qL
ct	2·5 (0·9)	0	0·29 (0·03)	anL – qL
fo	2·0 (0·7)	0	–0·03 (0·02)	foL
fa	–2·5 (1·5)	0	0·18 (0·02)	faL
hm	0·0 (0·3)	0	0·20 (0·01)	0·5 hemL
ek	21·0 (0·7)	0	0	0·5 eskL

thermodynamic dataset is provided as file tc-ds622.txt in the Supplementary Data, along with example files for running all phase equilibrium calculations here on KLB-1 composition, and a simple tutorial for using THERMOCALC. A recent version of THERMOCALC for OS X, Linux and Windows, and supporting files, may also be downloaded from http://www.esc.cam.ac.uk/research/research-groups/holland/thermocalc.

Melt

The melt model is discussed in the text. Non-ideal interactions are expressed in terms of regular solution energies $W_{i,j} = a + bT + cP$ (in kJ) for end-members *i* and *j*, as in Table A1. Approximate uncertainties are given in parentheses. Only the non-zero interaction energies are listed.

The enthalpies of end-members are those in the Holland & Powell (2011) dataset, with increments expressed as a difference ($\Delta_i = H_i - H_{i,\mathrm{ref}}$). Where an end-member *i* is made from a linear combination of others Δ_i is relative to that combination (Table A2). As before, the increment is expressed as $\Delta_i = a + bT + cP$ (in kJ), with approximate uncertainties from Monte Carlo runs given in parentheses.

The hemL (Fe_2O_3) component was calibrated by taking the known melting temperature of hematite as 1895°C (Robie *et al.*, 1978) with an estimate of entropy of melting of 44·9 J K^{-1}, which was made to agree with the log fO_2 in melts calibration of Jayasuriya *et al.* (2004) over the range 1075–1575°C. Volume, expansion and compressibility were from Kress & Carmichael (1991). Enthalpy was fitted to measured $Fe^{3+}/\Sigma Fe$ of basalts with low K_2O and low P_2O_5 of Kress & Carmichael (1991), where log fO_2 was calculated using the all-melt equilibrium $q + 4\ hm = 2fa + O_2$, using thermodynamic data and activity model presented here. The enthalpy of hm thus reproduces the experimental data over a range in log fO_2 from –8 to near zero and temperatures between 900 and 1500°C. Plots showing comparison with measured log fO_2 are provided in the Supplementary Data.

The eskL (Cr_2O_3) component properties were calibrated by taking known melting temperature 2265°C (Gaskell, 2012) with an estimate of entropy of melting of 50 J K^{-1}. Molar volume was estimated from corL + esk – cor. The heat capacity was assumed the same as corL (because C_p for cor and esk are almost identical). The enthalpy of the $CrO_{1.5}$ component was adjusted by + 21 kJ to make agreement with the Cr_2O_3 contents of partial melts (around 0·2 wt %) observed at 30 kbar by Takahashi (1986) and at 15 kbar by Hirose & Kushiro (1993).

Table A3: Clinopyroxene end-members in the model

	M2	M1	T
di	Ca	Mg	Si_2
cfs	Fe	Fe	Si_2
cats	Ca	Al	AlSi
crdi	Ca	Cr	AlSi
cess	Ca	Fe^{3+}	AlSi
jd	Na	Al	Si_2
cen	Mg	Mg	Si_2
cfm	Fe	Mg	Si_2

Plagioclase

Plagioclase feldspars are treated here as a simple asymmetric solution between anorthite and high albite, with Al–Si mixing allowed on only two of the four tetrahedral sites. Ideal activities are given by $a_{ab} = 4X_{Na}^{A}X_{Al}^{T}X_{Si}^{T}$ and $a_{an} = 4X_{Ca}^{A}(X_{Al}^{T})^2$. Non-ideal interaction is given by the asymmetric van Laar model, using the formalism of Holland & Powell (2003) with $W_{ab,an} = 22{\cdot}4$ kJ and asymmetry parameters $\alpha_{an} = 1{\cdot}0$ and $\alpha_{ab} = 0{\cdot}39$. These values come from fitting the enthalpy measurements of Newton *et al.* (1980).

Olivine

Olivines are treated as simple symmetric solid solutions between forsterite and fayalite, with $W_{fo,fa} = 9$ kJ for a two-site solution (e.g. Hackler & Wood 1989).

Clinopyroxene

Clinopyroxene is modelled after Green *et al.* (2012*a*) with additions for Fe, Na, Cr and Fe^{3+}. The end-members used are given in Table A3, with ideal activities being given by a mixing on sites model, in which the approach of Green *et al.* (2012*a*) is followed in reducing the T-site entropy of mixing to a quarter of the random value.

The non-ideality is expressed as an asymmetric van Laar model, using the formalism of Holland & Powell (2003). *W*, Δ_i and asymmetry parameters are given in Tables A4 and A5. *W* values involving Fe, Fe^{3+}, Na and Cr end-members are determined using the approach of

Table A4: Interaction energies for mixing of clinopyroxene end-members (kJ)

W	*a*	*b*	*c*	*W*	*a*	*b*	*c*
di, cfs	20·0	0	0	cats, cess	2·0	0	0
di, cats	12·3	0	–0·1	cats, jd	6·0	0	0
di, crdi	8·0	0	0	cats, cen	45·7	0	–0·29
di, cess	8·0	0	0	cats, cfm	27·0	0	–0·1
di, jd	26·0	0	0	crdi, cess	2·0	0	0
di, cen	29·8	0	–0·03	crdi, jd	3·0	0	0
di, cfm	18·0	0	0	crdi, cen	48·0	0	0
cfs, cats	25·0	0	–0·1	crdi, cfm	36·0	0	0
cfs, crdi	34·0	0	0	cess, jd	3·0	0	0
cfs, cess	34·0	0	0	cess, cen	58·0	0	0
cfs, jd	24·0	0	0	cess, cfm	36·0	0	0
cfs, cen	7·0	0	0	jd, cen	40·0	0	0
cfs, cfm	4·0	0	0	jd, cfm	40·0	0	0
cats, crdi	2·0	0	0	cen, cfm	4·0	0	0

Powell *et al.* (2014). Symbols and values are explained in the melt section above.

Orthopyroxene

Orthopyroxene is also modelled after Green *et al.* (2012*a*) with *W* values involving Fe, Fe^{3+} and Cr end-members determined using the approach of Powell *et al.* (2014). The end-members used are given in Table A6. The non-ideality is expressed as an asymmetric van Laar model, which is given in Tables A7 and A8 with symbols and values as for clinopyroxene.

Garnet

Garnets are modelled as in the study by Holland *et al.* (2013), but with addition of ferric iron and chromium. Sodium and majorite were not considered as, with an upper limit of investigation of 60 kbar, these contributions are not significant. The model is a regular solution of pyrope, almandine, grossular, andradite and knorringite end-members. The thermodynamic data for end-members are from Holland & Powell (2011). The model interaction energies for garnet involve both within-site and cross-site energy terms, and are as follows (in kJ):[Setter: please arrange following equations in two columns with a single tab, as follows]

$W_{pygr} = 35 + 0{\cdot}10P$ (W_{MgCaM1})

$W_{pyalm} = 4 + 0{\cdot}10P$ (W_{MgFeM1})

$W_{grandr} = 2$ $(W_{Fe3AlM2})$

$W_{pyknor} = 2$ (W_{CrAlM2})

$W_{gralm} = 4 + 0{\cdot}10P$ (W_{FeCaM1})

$W_{pyandr} = 91 + 0{\cdot}0017T + 0{\cdot}032P$ $(-W_{CaAlMgFe3M1M2} + W_{Fe3AlM2} + W_{MgCaM1})$

$W_{grknor} = 47 - 0{\cdot}0338T + 0{\cdot}221P$ $(W_{CaAlMgCrM1M2} + W_{CrAlM2} + W_{MgCaM1})$

$W_{almandr} = 60 + 0{\cdot}0017T + 0{\cdot}032P$ $(-W_{CaAlFeFe3M1M2} + W_{Fe3AlM2} + W_{FeCaM1})$

$W_{almknor} = 6{\cdot}0 + 0{\cdot}01P$ $(-W_{CaAlFeCrM1M2} + W_{CaAlMgCrM1M2} + W_{CrAlM2} + W_{MgFeM1})$

$W_{andrknor} = 101 - 0{\cdot}0321T + 0{\cdot}153P$ $(W_{CaAlMgCrM1M2} - W_{CaAlMgFe3M1M2} + W_{CrFe3M2} + W_{MgCaM1})$.

Table A5: Increments (in kJ) to Gibbs energies, and asymmetry parameters for mixing, of clinopyroxene end-members

Δ_i	*a*	*b*	*c*	Ref.	α
di	—	—	—	—	1·2
cfs	3·8	–0·003	0·03	fs	1·0
cats	—	—	—	—	1·9
crdi	–3·0	0	0	cats + kos – jd	1·9
cess	–6·0	0	0	cats + acm – jd	1·9
jd	—	—	—	—	1·2
cen	3·5	–0·002	0·048	en	1·0
cfm	–3·0	0	0	(en + fs)/2	1·0

Table A6: Orthopyroxene end-members in the model

	M2	M1	T
en	Mg	Mg	Si_2
fs	Fe	Fe	Si_2
fm	Fe	Mg	Si_2
odi	Ca	Mg	Si_2
mgts	Mg	Al	AlSi
cren	Cr	Mg	AlSi
mess	Mg	Fe^{3+}	AlSi

Table A7: Interaction energies for mixing of orthopyroxene end-members (kJ)

W	*a*	*b*	*c*	*W*	*a*	*b*	*c*
en, fs	5·2	0	0	fm, odi	18·0	0	0
en, fm	4·0	0	0	fm, mgts	2·0	0	–0·15
en, odi	32·2	0	0·12	fm, cren	12·0	0	0
en, mgts	13·0	0	–0·15	fm, mess	12·0	0	0
en, cren	8·0	0	0	odi, mgts	75·4	0	–0·94
en, mess	8·0	0	–0·03	odi, cren	30·0	0	0
fs, fm	4·0	0	0	odi, mess	30·0	0	0
fs, odi	24·0	0	0	mgts, cren	2·0	0	0
fs, mgts	7·0	0	–0·15	mgts, mess	2·0	0	0
fs, cren	10·0	0	0	cren, mess	2·0	0	0
fs, mess	10·0	0	0				

Table A8: Increments (in kJ) to Gibbs energies, and asymmetry parameters for mixing, of orthopyroxene end-members

Δ_i	*a*	*b*	*c*	Ref.	α
en	—	—	—	—	1·0
fs	—	—	—	—	1·0
fm	–6·0	0	0	(en + fs)/2	1·0
odi	–0·1	0·00211	0·005	di	1·2
mgts	—	—	—	—	1·0
cren	3·0	0	0	mgts + kos – jd	1·2
mess	–15·0	0	0·15	mgts + acm – jd	1·0

The sources of the within-site terms are as follows: W_{MgFeM1} from Geiger *et al.* (1987), Hackler & Wood (1989) and Koziol & Bohlen (1992); W_{MgCaM1} from Newton *et al.* (1977), Wood (1988) and Ganguly *et al.* (1996); W_{CrAlM2} from Mattioli & Bishop (1984) and Wood & Kleppa (1984); W_{FeCaM1} from Geiger *et al.* (1987), Koziol (1990) and Pownceby *et al.* (1987); $W_{Fe3AlM2}$ from Holland & Powell (2011).

The source of all the cross-site terms (reciprocal reactions) listed below is the thermodynamic data for the end-members grossular, pyrope, almandine, skiagite and knorringite of Holland & Powell (2011) and the method outlined by Powell *et al.* (2014) with the assumption of a zero energy for FeFe + MgAl = MgFe + FeAl. The data for skiagite were derived from the experiments of Woodland & O'Neill (1993) using the reaction skiagite + hercynite = almandine + magnetite.

$$W_{CaAlMgFe3M1M2} = -53{\cdot}8-0{\cdot}0017T + 0{\cdot}068P$$
$$W_{CaAlFeFe3M1M2} = -53{\cdot}8-0{\cdot}0017T + 0{\cdot}068P$$
$$W_{CaAlMgCrM1M2} = 10{\cdot}2-0{\cdot}0338T + 0{\cdot}121P$$
$$W_{CaAlFeCrM1M2} = 10{\cdot}2-0{\cdot}0338T + 0{\cdot}121P.$$

Spinel

Spinel is modelled on the parameterization of Bryndzia & Wood (1990) as described in the text. The ideal activities are those of a random solution over the three sites (combined octahedral and tetrahedral). Thus, for example, the ideal activity of picrochromite ($MgCr_2O_4$) would be $a_{pcr} = (27/4)X_{Mg}X_{Cr}{}^2$. The non-ideal terms come from a regular solution with parameters listed in the text.